SEG Special Publications, no. 24, pp. 137–158

# Chapter 9

# Magmatism and Related Au-Cu Mineralization in the Hualgayoc Mining District, Northern Peru

M. Viala† and K. Hattori

*Department of Earth and Environmental Sciences, University of Ottawa, Ottawa, Ontario, Canada K1N 6N5*

## Abstract

The Hualgayoc district in the Cajamarca region of northern Peru experienced middle Miocene andesitic to rhyolitic magmatism and magmatic hydrothermal activity that produced Au and Cu mineralization, including the Cerro Corona porphyry Au-Cu, Tantahuatay high-sulfidation epithermal Au, and the AntaKori skarn Cu-Au-Ag deposits. We examined 32 samples from 22 units that encompass the entire igneous rock record in the district. Our new U-Pb dating of 454 zircon grains from these 22 igneous units yielded Concordia ages showing continuous magmatic activity in the district, from 14.8 to 9.7 Ma. Igneous activity in the eastern part of the district took place between 14.8 and 14.0 Ma, including the Cerro Corona intrusive complex that hosts a porphyry Au-Cu deposit. Magmatism in the western part of the district occurred between 13.7 and 11.5 Ma and included the Tantahuatay Volcanic Complex that hosts a high-sulfidation Au deposit. The different styles of mineralization and ages of igneous rocks in the eastern and western parts are accounted for by deeper erosion to the east. Bulk-rock compositions indicate that parental magmas originated from amphibole-rich juvenile lithospheric mantle or lower crust and evolved through amphibole fractional crystallization. Amphibole and zircon compositions indicate that parental magmas of all igneous units in the Hualgayoc district were water-rich, >3 wt % $H_2O$, and oxidized above the fayalite-magnetite-quartz (FMQ) redox buffer. Our observations in the Hualgayoc district suggest that oxidized conditions and high-water contents are necessary to produce porphyry-type mineralization, but that other factors were also critical to form mineralization, such as a shallow depth of magma emplacement, with near-vertical shape of intrusions. These findings are likely applicable elsewhere.

## Introduction

Porphyry-style Cu ± Au and high-sulfidation Au deposits are major global sources of Cu and Au (Sillitoe, 2010). The Cajamarca region in the northern Peruvian Cordillera (Fig. 1) hosts numerous Miocene porphyry-style Cu-Au and high-sulfidation epithermal Au deposits. These include deposits in the Yanacocha district, the world's largest high-sulfidation Au cluster (Harvey et al., 1999; Longo et al., 2010), with >1,200 metric tons (t) Au production. The Hualgayoc district is located in the northern part of the Cajamarca region, 30 km north of Yanacocha (Fig. 1), and has been historically important for Ag production (Gustafson et al., 2004). The district hosts the Cerro Corona Au-Cu porphyry deposit, the Tantahuatay high-sulfidation Au deposit, the AntaKori Cu-Au-Ag skarn deposit, and several Au, Cu, Ag, and base metal prospects (tonnage and grades are listed in Table 1); the first two deposits are being mined as of 2021. The district also contains many apparently barren igneous rocks that are unaltered to moderately altered, with the only sulfide being pyrite. Since these mineralized and barren rocks are broadly contemporaneous and similar in lithology and mineralogy, the district provides an opportunity to evaluate critical characteristics of magmas that are related to the formation of porphyry and high-sulfidation ore deposits.

† Corresponding author: e-mail, martin.viala@me.com

The most recent examination of the geology and petrology of the Hualgayoc district was by Gustafson et al. (2004), aside from a publication by Viala and Hattori (2021) that evaluates Ce and Eu anomalies of zircon grains as possible fertility indicators. This paper presents new U-Pb zircon ages of igneous rock units in the Hualgayoc district, integrates them with the mineralogy, mineral chemistry, and bulk-rock compositions of 32 samples and historic data from the Cajamarca region, and discusses magma sources, the evolution of magmatism, and parameters related to mineralization.

## Geologic Setting

### *Tectonic and magmatic history of the Cajamarca region*

The Hualgayoc district (Fig. 1) is located at an elevation of ~4,000 m in the northern Peruvian Andes. Northern Peru hosts four principal trench-parallel (NW-SE) terranes: the Coastal belt, the Western Cordillera, the Marañon fold thrust belt, and the Eastern Cordillera. The Coastal belt consists of coastal batholiths of Upper Cretaceous to Paleocene ages (Mukasa and Tilton, 1984; Cobbing, 1999). The Western Cordillera is composed of Cretaceous to Tertiary dioritic to monzonitic batholiths that intruded Precambrian to Paleozoic metasedimentary rocks and Ordovician to Upper Cretaceous siliciclastic and carbonate sedimentary rocks (Wilson, 1984; Scherrenberg et al., 2012). The Eastern Cordillera is separated from the Western Cordillera by the Marañon fold

Open Access (CC-BY-NC) publication of the Jeremy P. Richards memorial volume was generously supported by BHP Metals Exploration and the Laurentian University Mineral Exploration Research Centre (MERC) and Harquail School of Earth Sciences (HES).

Digital Appendix 1 follows the text. Additional Appendices are available online at www.segweb.org/SP24-Appendices.
doi: 10.5382/SP.24.09; 22 p.

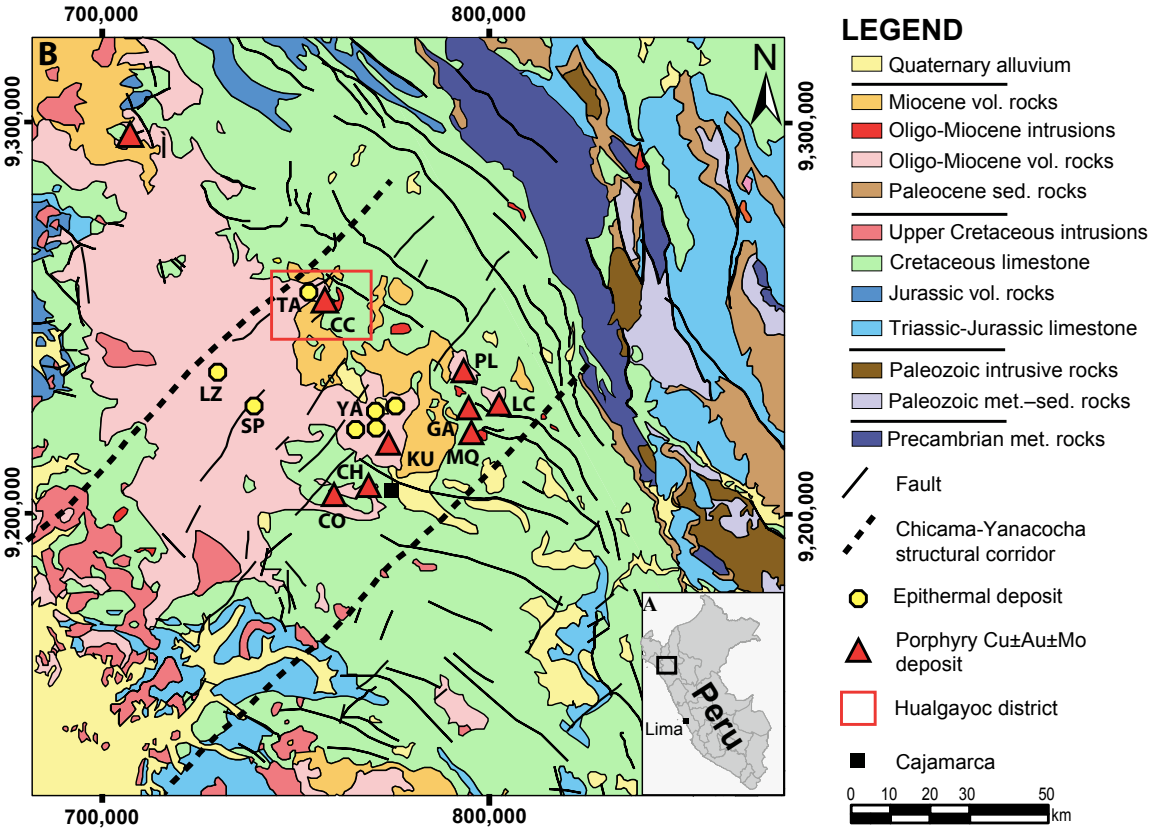


Fig. 1. Geologic map of the Cajamarca region, showing the locations of major porphyry Cu ± Au and high-sulfidation Au deposits. Inset (A) shows the region location (black square) in northern Peru. The Hualgayoc district (red square) is located 30 km north of the Yanacocha district. CC = Cerro Corona, CH = Chamis, CO = Colpayoc, GA = El Galeno, KU = Kupfertal, LC = La Carpa, LZ = La Zanja, MQ = Michiquillay, PL = Perol, SP = Sipan, TA = Tantahuatay, YA = Yanacocha. Modified after Brewer and Davis (2004). UTM coordinates (m) are WGS84 Zone 17S.

thrust belt and consists of Paleozoic metasedimentary rocks intruded by Ordovician to Triassic granitoids (Mišković et al., 2009).

The Cajamarca region is located in the northern part of the Western Cordillera (Fig. 1). The crystalline basement of Precambrian age is overlain by a thick (> 2 km) Upper Jurassic to Lower Cretaceous sequence of siliciclastic sedimentary rocks at the base, and a ~1,500-m-thick package of Upper Cretaceous limestone and shales (Benavides-Cáceres, 1956; Wilson, 1984). These sedimentary rocks are overlain by Eocene to Miocene intermediate to felsic volcanic rocks and are intruded by numerous mafic to felsic bodies of similar ages (Gustafson et al., 2004; Longo et al., 2010; and references therein). These young igneous rocks formed in response to the easterly subduction of the Farallon oceanic plate and later Nazca oceanic plate. The sedimentary rocks were deformed during two periods of Tertiary tectonism in the northern Peruvian Andes: the Inca orogeny during the Paleocene to Miocene, and the Quechua orogeny during the Miocene to Pliocene (Mégard, 1984; Noble et al., 1990; Benavides-Cáceres, 1999). These previous workers recognized four pulses of crustal shortening and magmatic activity during the Inca orogeny, and three pulses during the Quechua orogeny: Inca I (59–55 Ma), Inca II (44–43 Ma), Inca III (26 Ma), and Inca IV (22 Ma), and Quechua I (17 Ma), Quechua II (8–7 Ma), and Quechua III (7-4 Ma).

Two major magmatic episodes are recorded in the Cajamarca region. The oldest occurred during the Paleogene (57–35 Ma) and produced a thick sequence of basaltic to andesitic volcanic rocks (Noble et al., 1990), and apparently barren intermediate intrusions of Cocañes East (43.6 ± 3.7 Ma; Llosa et al., 1996), the Picota Diorite (43.6 Ma; Laughlin et al., 1968), Cerro Montana (47 ± 3 Ma), La Carpa (42.55 ± 0.12 Ma), and Cerro Perol East (57 ± 3 Ma) (Davies, 2002). Magmatic activity decreased from 36 to 24 Ma, due to a decrease in the convergence rate of the Farallon plate (Pardo-Casas and Molnar, 1987). The second major magmatic activity in the Cajamarca region occurred during the Miocene, 23 to 7 Ma, shortly after the breakup of the Farallon plate to become the Nazca and Cocos plates at ~25 Ma (Barckhausen et al., 2008), followed by rapid subduction of the Nazca plate (Pardo-Casas and Molnar, 1987).

Early- to middle-Miocene magmatic activity, from 23 to 15 Ma, resulted in andesitic and dacitic volcanic eruption of the Calipuy Group rocks in the Yanacocha district between 19.5 and 15.1 Ma (Longo et al., 2010, and references therein). Note that the Calipuy Group rocks are the oldest unit in the Yanacocha district and different from volcanic rocks of the Calipuy Formation in the Hualgayoc district. Several porphyry Cu ± Au deposits formed in the southeastern part of the Cajamarca region at this time, including the Minas Congas group (23.2 ± 2.1–14.2 ± 1.3 Ma; Llosa et al., 1999), with largest

Table 1. Tonnage and Grade Data of Deposits from the Cajamarca Region, and Ages of Mineralization

| Deposit name[1] | Deposit type | Host rock | Age of mineralization (Ma) | Tonnage (Mt) | Grade | | Comment |
|---|---|---|---|---|---|---|---|
| | | | | | Cu (wt%) | Au (g/t) | |
| Hualgayoc district | | | | | | | |
| Cerro Corona | Porphyry Au-Cu | Dioritic intrusions | ~14.5 Ma [14] | 110 [1] | 0.5 [1] | 0.9 [1] | 54.4 t Au, 0.37 Mt Cu produced, 2009-2019 [4] |
| Tantahuatay | High-sulfidation Au-Ag | Andesitic to rhyolitic volcanic and pyroclastic rocks; shallow porphyritic intrusions | 13.3-11.01 Ma [9] | 225 [1] | – | 0.33 [1] | 23.8 t Au produced, 2014-2018 [6] |
| AntaKori | Skarn Cu-Au-Ag | Limestone | > 12.4 Ma [5] | 517 [5] | – | – | Indicated and inferred resources consist of 2.3 Mt Cu and 140 t Au (2019) [5] |
| Cajamarca region | | | | | | | |
| Minas Conga | Porphyry Au-Cu | Dioritic intrusions [8] | 16.06–15.58 [13] | 641 [1] | 0.28 [1] | 0.75 [1] | |
| El Galeno | Porphyry Cu-Au | Dioritic intrusions [8] | 17.5–16.5 [8] | 486 [8] | 0.57 [8] | 0.14 [8] | 115 ppm Mo [8] |
| Michiquillay | Porphyry Cu | Dioritic intrusions [8] | 19.77±0.05 [8] | 631 [8] | 0.69[8] | 0.15 [8] | 100-200 ppm Mo [8] |
| Sipan | High-sulfidation Au-Ag | Andesitic volcanic rocks [10] | 13.3 [11] | 16 [1] | – | 2 [1] | ~30 t Au in oxide zone mined before 2001 [1] |
| La Zanja | High-sulfidation Au-Ag | – | 15.61±0.12 [12] | 33 [1] | – | 0.69 [1] | 19.4 t Au produced, 2014-2018 [6] |
| Yanacocha district | High-sulfidation Au-Ag | Dacite to andesitic igneous rocks [2] | 13.5–8.2 [2] | – | 0.63 [1] | 0.98 [1] | 1225 t Au produced, 1993–2010 [2]; 81.2 t 2015-2018; proven and probable reserves in 2019: 216 t Au (oxide and sulfide), 0.66 Mt Cu (sulfide) [7] |

References: [1] Miguel Cardozo (pers. commun., 2020); [2] Longo et al. (2010); [3] Candiotti and Guerrero (1997); [4] https://www.goldfields.com; [5] https://regulusresources.com/projects/resource/; [6] www.buenaventura.com; [7] www.miningdataonline.com; [8] Davies and Williams (2005); [9] Prihar (1998), Table A2-8 in the App. 2; [10] Candiotti and Guerrero (1997); [11] Noble and McKee (1997); [12] Noble et al. (2004); [13] Gustafson et al., 2004; [14] this study

[1]Locations are shown in Figure 1

deposit at Michiquillay (20.02 ± 0.15–19.77 ± 0.04 Ma; Noble et al., 2004; Davies and Williams, 2005), El Galeno (17.5 ± 0.3–16.53 ± 0.18 Ma; Davies and Williams, 2005), and Perol (15.96 ± 0.20; Gustafson et al., 2004). Several barren intrusions were emplaced during the same period, including those of Aurora Patricia (21.3 ± 0.8 Ma; Davies, 2002), Michiquillay north (20.6 ± 0.4 Ma; Davies and Williams, 2005), and La Carpa (17.85 ± 0.06 Ma; Davies, 2002).

Magmatic-hydrothermal activity in the Hualgayoc district started at ~15 Ma and lasted until ~11 Ma, with minor felsic domes extruded until ~9 to 8 Ma. Magmatic-hydrothermal activity in the Yanacocha district, located ~30 km south-southeast of the Hualgayoc district, started at ~16 Ma and continued until ~11 Ma, with minor dome extrusion until ~8 Ma (Longo et al., 2010). The oldest high-sulfidation deposit of the Yanacocha district formed at 13.5 Ma, and the youngest and largest deposit, Cerro Yanacocha, formed between 9.3 to 8.2 Ma (Longo et al., 2010). Cessation of major magmatic activity in the Cajamarca region occurred at ~8 Ma.

### *Geology of the Hualgayoc district*

The Hualgayoc district is largely underlain by weakly folded Cretaceous limestone and minor sandstone, intruded by Miocene igneous rocks (Fig. 2). The stratigraphy of the district was described in detail by Benavides-Cáceres (1956) and Wilson (1963). The rocks were under compression, resulting in the formation of several NW-SE- and NE-SW-trending thrust faults during the Inca orogeny (Benavides-Cáceres, 1999). These faults were reactivated during the Quechua orogeny in the middle Miocene, again under regional compression (Benavides-Cáceres, 1999). In the western part of the Hualgayoc district, the Cretaceous sedimentary rocks are intruded by porphyritic rocks and overlain by andesitic to rhyolitic flows, domes, and tuffs of the Calipuy Formation. The eastern and northwestern parts of the district are dominated by amphibole ± biotite ± quartz diorite porphyry, including the Cerro Corona intrusive complex, the Coymolache sill, the Cerro Jesus, Cerro San Jose, Cerro Las Gordas, Cerro Caballerisa, Cerro Choro Blanco, San Nicolas, and the San Miguel intrusions, plus the Hualgayoc rhyodacite dome located north of Cerro Jesus (Fig. 2). These igneous units are listed in Table 2.

### *Mineralization and alteration in the Hualgayoc district*

The Hualgayoc district hosts several styles of mineralization, formed between 15 and 11 Ma (Macfarlane and Petersen, 1990; Macfarlane et al., 1994; Noble and McKee, 1999). They include porphyry Au-Cu mineralization at Cerro Corona, high-sulfidation epithermal Au mineralization at Tantahuatay, and skarn Cu-Au-Ag mineralization in the AntaKori area. Minor occurrences of Pb-Zn-Cu-Ag veins and mantos were reported near the Hualgayoc village by Macfarlane (1989), and there are numerous Ag veins in the district (Fig. 2).

Table 2. Lithology, Mineralogy, Alteration, Age, and Location of Samples in the Hualgayoc District

| Sample no. | Igneous unit | Abbreviations in the map | Sample location[1] Easting (m) | Northing (m) | Lithology |
|---|---|---|---|---|---|
| CC1 | Cerro Corona Phase 1 | CC | 762,812 | 9,252,019 | Qz-diorite porphyry |
| CC4 | Cerro Corona Phase 4 | | 763,296 | 9,251,870 | Qz-diorite porphyry |
| CC4b | | | 763,281 | 9,251,816 | Qz-diorite porphyry |
| CC5 | Cerro Corona Phase 5 | | 762,934 | 9,251,586 | Qz-diorite porphyry |
| CC5n | | | 762,951 | 9,251,723 | Qz-diorite porphyry |
| CC6 | Cerro Corona Phase 6 | | 763,085 | 9,251,843 | Qz-diorite porphyry |
| SJD-05 | San Jose | SJ | 764,830 | 9,251,099 | Qz-diorite porphyry |
| SJD-02 | | | 765,137 | 9,251,308 | Qz-diorite porphyry |
| 25-4 | | | 765,119 | 9,251,258 | Altered porphyry |
| Tanta-352 | Tantahuatay-2 intrusion A | TA | 757,458 | 9,255,461 | Altered porphyry |
| Tanta-355 | Tantahuatay-2 intrusion B | | 758,118 | 9,255,898 | Altered porphyry |
| Tanta-356 | Tantahuatay-2 intrusion C | | 758,015 | 9,255,942 | Altered porphyry |
| Tanta-357 | Tantahuatay-2 intrusion D | | 758,008 | 9,255,855 | Altered porphyry |
| Tanta-358 | Tantahuatay-Cienaga intrusion A | CNG | 754,547 | 9,254,613 | Altered porphyry |
| CNG-1 | Tantahuatay-Cienaga intrusion B | | 754,389 | 9,253,072 | Altered Pl porphyry |
| Anta-PK# | PK porphyry dike | AK | 758,093 | 9,256,788 | Altered Pl-Qz-Bt porphyry |
| Anta-PF * | Calipuy subvolcanic intrusion 1 | | 758,116 | 9,256,564 | Altered Qz-Pl porphyry |
| Anta-6 | | | 757,858 | 9,256,301 | Altered Qz-Pl porphyry |
| Anta-8 | Calipuy rhyolite dome§ | | 758,236 | 9,256,684 | Rhyolite |
| CJ | Cerro Jesus | JE | 764,114 | 9,252,182 | Qz-diorite porphyry |
| 25-7 | | | 763,832 | 9,252,892 | Qz-diorite porphyry |
| 18-2 | | | 765,179 | 9,252,480 | Qz-diorite porphyry |
| CB | Cerro Choro Blanco | CB | 760,586 | 9,251,265 | Diorite porphyry |
| CAB | Cerro Caballerisa | CAB | 760,244 | 9,251,364 | Diorite porphyry |
| LG | Las Gordas | LG | 760,081 | 9,252,023 | Silicified intrusive rock |
| CD | Coymolache | CO | 761,877 | 9,249,776 | Qz-diorite porphyry |
| 25-5 | | | 763,733 | 9,249,006 | Qz-diorite porphyry |
| SCO-1 | San Miguel | SM | 759,532 | 9,256,283 | Qz-diorite porphyry |
| SCO-2 | | | 759,214 | 9,256,907 | Qz-diorite porphyry |
| SCO-3 | | | 758,993 | 9,257,411 | Qz-diorite porphyry |
| SN | San Nicolas | SN | 760,473 | 9,253,673 | Qz-diorite porphyry |
| 25-6 | Hualgayoc | HG | 764,213 | 9,253,208 | Rhyodacite |

Abbreviations: Aln = alunite, Anh = anhydrite, Bt = biotite, Ccp = chalcopyrite, Chl = chlorite, Dsp = diaspore, Ep = epidote, Hbl = hornblende, Ilm = ilmenite, Kal = kaolinite, Kfs = potassic feldspar, Mag = magnetite, Pl = plagioclase, Prl = pyrophyllite, Py = pyrite, Qz = quartz, Ttn = titanite, WM = white mica, Zrn = zircon

[1] UTM coordinates are WGS84 Zone 17M

[2] Ages are weighted means of the $^{206}Pb/^{238}U$ zircon ages; uncertainties are 2 sigma values

[3] Age of the San Jose intrusion obtained from zircon grains in samples of SJD-02 and 24-4, that for the San Miguel intrusion from samples of SCO-1, SCO-2, and SCO-3

*PF refers to quartz-feldspar porphyry, corresponding to multiple bodies of Calipuy subvolcanic intrusion 1 in Figure 4; note that the Calipuy Formation rocks in the Hualgayoc district are different from older Calipuy Group rocks in the Yanacocha district

# PK is an older porphyry containing phenocrysts of feldspar, quartz, and biotite, corresponding to small dikes associated with Early Breccia unit in Figure 4

§ Anta-8: this corresponds to felsic dome in Figure 4

The Cerro Corona deposit is located 2 km west of the Hualgayoc village in the central part of the district (CC, Fig. 2). The deposit is hosted by multiple quartz-diorite intrusions emplaced in Cretaceous limestone, forming a roughly circular intrusive complex 1 km in diameter (Fig. 3). At least six separate intrusive phases, with intrusive contacts against earlier units, have been mapped by mine geologists (Uzategui-Obando, 2016; Fig. 3). All intrusive phases have similar mineralogy and mineral abundances, containing plagioclase, amphibole, biotite, and quartz phenocrysts, with microphenocrysts of apatite, zircon, magnetite, and ilmenite. Disseminated hydrothermal biotite forms small light brown flakes in the groundmass or replacing dark brown primary biotite and amphibole phenocrysts, with magnetite cubes after biotite and amphibole phenocrysts; pink K-feldspar is present as an alteration halo to quartz veins. This potassic alteration is overprinted by chlorite + white mica + pyrite alteration at shallower depths in the deposit. The latest alteration of illite ± smectite ± kaolinite overprints earlier alteration styles in the upper part of the deposit. Mineralization associated with potassic alteration consists of chalcopyrite and bornite related to the stockwork veins of quartz + calcite ± magnetite ± hematite ± pyrite. The geology of the deposit and the distribution of different alteration types are described in detail by Longridge (2016). Potassic alteration and chalcopyrite veinlets are present locally in the nearby San Jose intrusion (SJ, Fig. 2).

The Tantahuatay Volcanic Complex is located 5 km west of the Cerro Corona deposit (Fig. 2), with poor outcrop exposure due to the cover of young volcanic rocks of the Calipuy Formation (Fig. 4). The Tantahuatay Complex is composed of numerous andesitic to rhyolitic flows and domes, plus porphyry plugs and dikes. The complex hosts the Tantahuatay high-sulfidation Au deposit, with Au mineralization in two major zones: the Tantahuatay-2 zone and the Cienaga zone (TA and CNG, respectively; Fig. 2). Nearly all igneous rocks in the Tantahuatay area have pervasive quartz ± alunite ± pyrophyl-

Table 2. *(Cont.)*

| Sample no. | Primary minerals | Intensity of alteration and alteration minerals | Zircon $^{206}Pb/^{238}U$ age (Ma)[2] |
|---|---|---|---|
| CC1 | Bt, Hbl, Pl, Qz, Ap, Mag, Ilm, Zrn | Weak – Bt, Kfs, Mag, Chl | 14.57 ± 0.16 |
| CC4 | Bt, Hbl, Pl, Qz, Ap, Mag, Ilm, Zrn | Moderate – Bt, Kfs, Mag, Chl | 14.40 ± 0.28 |
| CC4b | Bt, Hbl, Pl, Qz, Ap, Mag, Ilm, Zrn | Moderate – Bt, Kfs, Mag, Chl | 14.51 ± 0.21 |
| CC5 | Bt, Hbl, Pl, Qz, Ap, Mag, Ilm Zrn | Moderate – Bt, Kfs, Mag, Chl | 14.42 ± 0.20 |
| CC5n | Bt, Hbl, Pl, Qz, Ap, Mag, Ilm, Zrn | Moderate – Bt, Kfs, Mag, Chl | 14.40 ± 0.12 |
| CC6 | Bt, Hbl, Pl, Qz, Ap, Mag, Ilm, Zrn | Moderate – Bt, Kfs, Mag, Chl | 14.59 ± 0.13 |
| SJD-05 | Bt, Hbl, Pl, Qz Ilm, Zrn | Moderate – Bt, Kfs, Mag, Chl | – |
| SJD-02 | Bt, Hbl, Pl, Qz, Zrn | Intense – WM, clay minerals | 14.73 ± 0.13[3] |
| 25-4 | Qz (residual), Zrn | Intense – WM, Clay minerals | |
| Tanta-352 | Qz (residual), Zrn | High to intense – Qz±Aln±Prl | 13.09 ± 0.27 |
| Tanta-355 | Qz (residual), Zrn | High to intense – Qz±Aln±Prl | 12.91 ± 0.56 |
| Tanta-356 | Qz (residual), Zrn | High to intense – Qz±Aln±Prl | 12.64 ± 0.56 |
| Tanta-357 | Qz (residual), Zrn | High to intense – Qz±Aln±Prl | 12.46 ± 0.49 |
| Tanta-358 | Pl, Qz, Zrn | High – WM | 14.06 ± 0.49 |
| CNG-1 | Zrn | Intense – Qz±Aln | 14.52 ± 0.49 |
| Anta-PK[#] | Pl, Qz, Bt, Zrn | High – WM | 14.44 ± 0.25 |
| Anta-PF [*] | Pl, Qz, Bt, Ttn, Zrn | High – WM | 12.01 ± 0.26 |
| Anta-6 | Pl, Qz, Hbl, Zrn | Intense – Prl, Kal, Dsp | 13.18 ± 0.37 |
| Anta-8 | Pl, Qz, Kfs, Hbl, Zrn | Moderate – WM | 11.51 ± 0.37 |
| CJ | Pl, Hbl, Qz, Zrn | High – WM | – |
| 25-7 | Pl, Hbl, Qz, Zrn | High – WM | 14.83 ± 0.36 |
| 18-2 | Pl, Hbl, Qz, Zrn | Weak – Chl, Ep | – |
| CB | Pl, Hbl, Qz, Zrn | None | 14.22 ± 0.25 |
| CAB | Pl, Hbl, Qz, Zrn | None | 14.11 ± 0.18 |
| LG | Zrn | Intense – Qz, WM | 14.35 ± 0.28 |
| CD | Pl, Hbl, Bt, Qz, Kfs, Mag, Zrn | Weak – Chl | – |
| 25-5 | Pl, Hbl, Bt, Qz, Kfs, Mag, Zrn | Weak – Chl | 14.32 ± 0.28 |
| SCO-1 | Pl, Hbl, Bt, Qz, Kfs, Mag, Ilm, Zrn | Weak to moderate – Chl, Ep | 14.52 ± 0.14[3] |
| SCO-2 | Pl, Hbl, Bt, Qz, Kfs, Mag, Ilm, Zrn | Weak to moderate – Chl, Ep | |
| SCO-3 | Pl, Hbl, Bt, Qz, Kfs, Mag, Ilm, Zrn | Weak to moderate – Chl, Ep | |
| SN | Pl, Hbl, Bt, Mag, Zrn | Weak – Chl, Ep | 13.67 ± 0.28 |
| 25-6 | Bt, Pl, Kfs, Qz, Zrn | None | 9.74 ± 0.31 |

lite alteration (Fig. 5C, D) and local residual quartz. "Gusano" (wormy) texture of nodular patches of alunite ± pyrophyllite ± diaspore that replaced the quartz matrix is common. Drilling intersected brecciated porphyritic rocks with fragments containing secondary K-feldspar and biotite (Jose Trujillo, pers. commun., 2017; Stewart Redwood, pers. commun., 2017), indicating the presence of high-temperature potassic alteration beneath the Tantahuatay deposit. Gold is mostly associated with enargite ± digenite ± covellite in quartz veins, disseminations or breccia fill, as well as in local supergene oxidized zones over the sulfide mineralization (Gustafson et al., 2004). The gold-bearing supergene oxide zones at Tantahuatay are not as well developed as in the Yanacocha deposits, possibly due to a greater degree of erosion in the Hualgayoc district.

The AntaKori deposit (AK; Fig. 2) is located ~500 m north of the Tantahuatay-2 zone. The geology consists of several porphyritic subvolcanic intrusions, including the PK porphyry dike and volcanic rocks of the Calipuy Formation (Fig. 4B). The deposit consists of Cu-Au-Ag mineralization of garnet skarns in Cretaceous limestone, and Cu-Au-Ag ± Mo porphyry mineralization (Redwood et al., 2017; Eggleston et al., 2019). These two styles of mineralization were overprinted by high-sulfidation Au mineralization and alteration, apparently extending from the Tantahuatay area.

The Coymolache sill, the Cerro Jesus, Cerro Las Gordas, Cerro Caballerisa, Cerro Choro Blanco, San Nicolas, and San Miguel intrusions plus the Hualgayoc rhyodacite dome are not known to be associated with mineralization and are therefore considered barren. Weak to moderate alteration of ferromagnesian igneous minerals to chlorite ± epidote occurs in the Coymolache sill, and the Cerro Caballerisa, Cerro Choro Blanco, Cerro Jesus, San Nicolas, and San Miguel intrusions. Pervasive white-mica alteration is present in the San Jose intrusion and locally in the Cerro Jesus intrusion. Residual quartz and quartz-stockwork veinlets are present in the Las Gordas intrusion. The Cerro Hualgayoc rhyodacite is not altered.

## Samples

We conducted fieldwork in 2016 and 2017 in the Hualgayoc district and collected 15 igneous rock units from their outcrops, six rock samples from two operating mines, and 11 drill core samples. In total, 32 rock samples from 22 different igneous units were examined for this study, encompassing most known rock units in this district. Samples from the Cerro Corona open pit include phase 1 (CC1), two samples of phase 4 (CC4 and CC4b), two samples of phase 5 (CC5 and CC5n), and one sample from phase 6 (CC6; Fig. 3). Two drill core samples from the San Jose intrusion, SJD-02 and SJD-05, were provided by Gold Fields La Cima S.A. Five drill core samples, Tanta-352, -355, -356, -357, and -358, were collected from the Tantahuatay mine, and one outcrop sample, CNG-1, with access provided by Compañía de Minas Buenaventura S.A.A. (Fig. 4). Drill core samples from the AntaKori area, Anta-PK, Anta-PF, Anta-6, and Anta-8, were collected at the Cajamarca drill core storage of Regulus Resources Inc. A total of 15 intrusion samples were collected from outcrops,

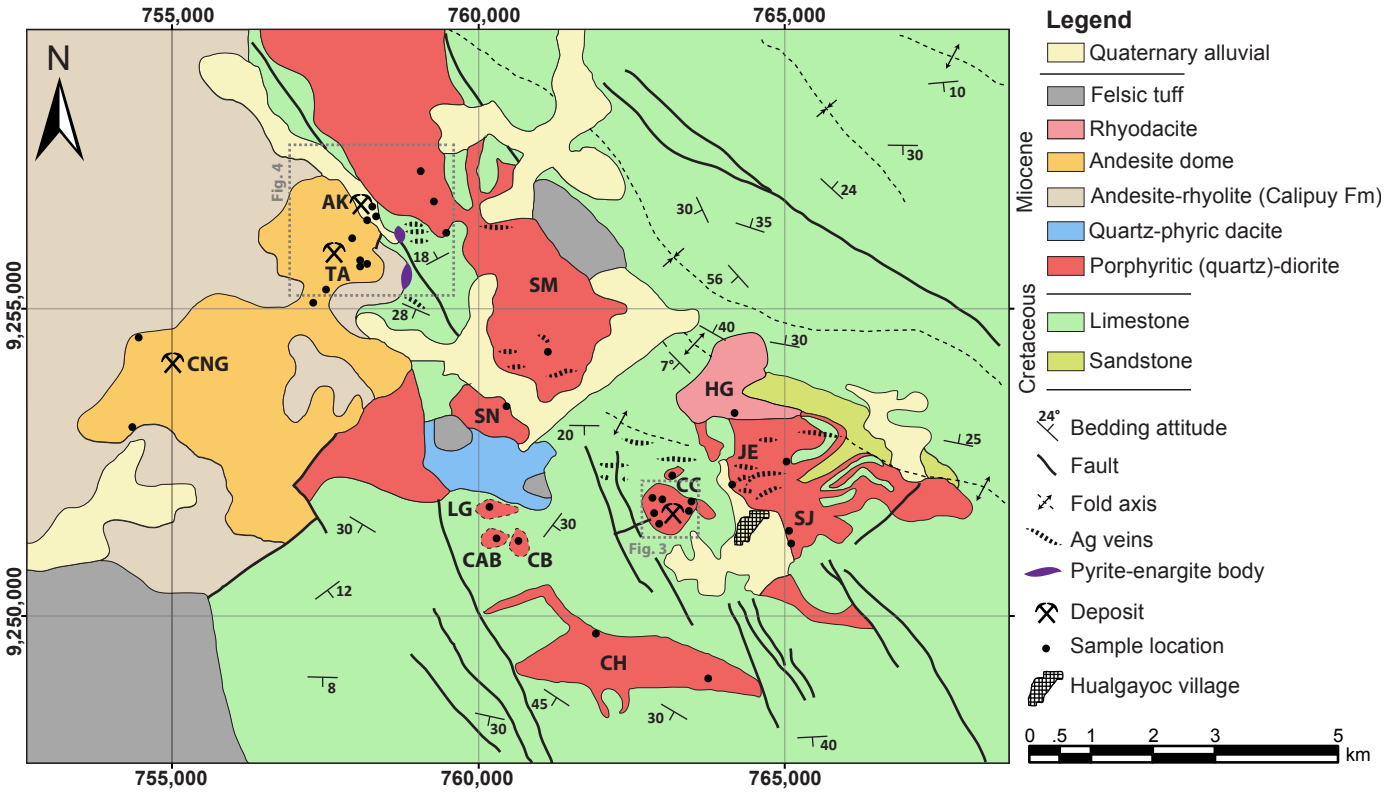


Fig. 2. Simplified geologic map of the Hualgayoc district, showing sample locations and igneous units. Abbreviations: AK = AntaKori intrusions, CAB = Caballerisa, CB = Choro Blanco, CC = Cerro Corona, CH = Coymolache, CNG = Cerro Cienaga, HG = Hualgayoc, JE = Cerro Jesus, LG = Las Gordas, SJ = San Jose, SM = San Miguel, SN = San Nicolas, TA = Tantahuatay 2. Modified after S. Canchaya, J. Paredes, and R. Tosdal (1996), cited by Gustafson et al. (2004), with intrusions in the AntaKori area added. Gray dashed rectangle corresponds to the map area in Figures 3 and 4.

including the Cerro Jesus, Cerro San Jose, San Miguel, Cerro Las Gordas, Cerro Choro Blanco, and Cerro Caballerisa intrusions, the Coymolache sill and the Hualgayoc rhyodacite. The coordinates of sampling locations are listed in Table 2 and are marked with solid black dots in Figures 2, 3, and 4. These samples are described in Viala and Hattori (2021), with their petrographic features and mineralogy summarized in Table 2.

## Analytical Methods

We selected 31 samples for bulk-rock analysis. The abundance of major and minor elements was measured using a Rigaku Supermini 200 wavelength dispersive X-ray fluorescence spectrometer (XRF) on fused glass of pulverized samples after mixing with lithium metaborate and lithium tetraborate at the University of Ottawa. The abundances of trace elements, including REE, were determined by Actlabs (analytical code 4LITHOS) in Ancaster, Ontario, Canada. Fused samples with sodium peroxide were dissolved in nitric and hydrochloric acids. The resulting solutions were diluted and analyzed using an Agilent 7900 inductively coupled plasma-mass spectrometer (ICP-MS) and a Varian 735ES inductively coupled plasma-optical emission spectrometer (ICP-OES).

Zircon grains were separated from most samples with the conventional method of magnetic and density separation using di-iodomethane (3.3 g/cm$^3$). Over 100 zircon grains were collected from individual rock units, with clear grains handpicked under a binocular microscope and then mounted in epoxy resin. Most grains are euhedral prismatic crystals with length/width ratios ranging from 1.5 to 3. Grains were examined under a transmitted-light microscope and with a JEOL 6610LV scanning electron microscope (SEM) at the University of Ottawa. Analyzed grains are clear, free of fractures, and low in mineral inclusions. Most grains show fine, well-developed oscillatory growth zoning under cathodoluminescence (CL) on SEM (Fig. 6A-C). Inherited cores are rare, but easily identified in CL-SEM images due to corroded outline of the cores. Occurrence, textures, and physical and optical properties of zircon grains used in this study are essentially identical to those reported in Viala and Hattori (2021).

Trace element contents in zircon were obtained from 473 zircon grains from all 22 igneous units and Eu and Ce anomalies are reported by Viala and Hattori (2021). The U-Pb dates were determined from 10 to 26 zircon grains for each igneous unit. Trace element abundances and isotope compositions of Pb and U were determined at the University of Ottawa, using an Agilent 7700x ICP-MS coupled with a Photon Machines Analyte Excite 193 nm excimer laser. For each grain, we chose an analysis area as close as possible to the rim of grains in order to avoid the mineral inclusion-rich center of the grains. The presence of minute mineral inclusions was monitored using $^{42}$Ca, $^{54}$Fe, $^{31}$P, $^{88}$Sr, $^{139}$La, and $^{140}$Ce during the analysis. U-Pb ages were determined on the same instrument, except for samples CC1, CC4, CC4b, CC5, CC5n, and CC6. Ages of zircon from samples CC1, CC4, CC4b, CC5, CC5n, and

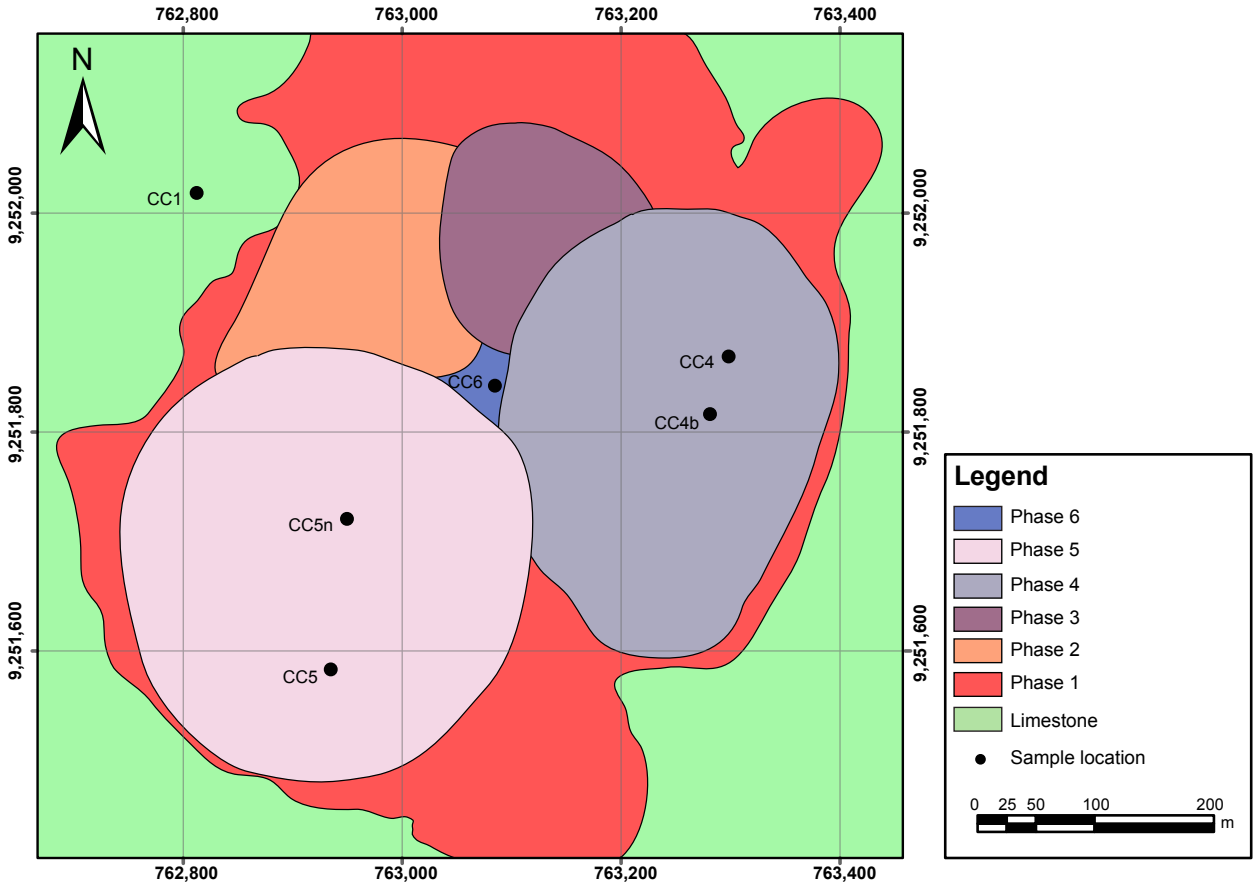


Fig. 3. Simplified geologic map of the Cerro Corona Intrusive Complex, provided by Gold Fields La Cima S.A. (2017).

CC6 were determined with the SHRIMPII at the Geochronological Laboratory of the Geological Survey of Canada. The analytical methods are essentially similar to those described in Kobylinski et al. (2020), with details described in Appendix 1. Individual zircon ages were calculated from $^{206}Pb/^{238}U$ ratios using the IsoplotR software (Vermeesch, 2018), a modified program of the original *Isoplot* program by Ludwig (2003). Uncertainty is expressed as $2\sigma$ values.

Amphibole grains from sample SN of the San Nicolas intrusion and sample 25-5 of the Coymolache sill were examined by SEM to select three grains from the former and four from the latter, with compositions of four areas of each grain quantitatively determined with a JEOL 8230 electron probe microanalyzer at the University of Ottawa. Analytical conditions included accelerating voltage of 15 kV, beam current of 20 nA, and a focused beam size of 5 µm. Detailed descriptions of analytical methods are included in Appendix 1.

## Results

### *Bulk-rock composition*

Bulk-rock compositional data are listed in Table A2-2, Appendix 2. Most samples have $SiO_2$ contents that range from 59 to 61 wt %, with some samples from Cerro Corona, Cerro Jesus, and Cerro San Jose up to 67 wt % $SiO_2$ due to alteration. Sample SG from the Las Gordas intrusion, which consists mostly of residual quartz with minor clay minerals, shows the highest $SiO_2$ (75 wt %) among samples. Samples from the unmineralized and weakly to moderately altered San Miguel, San Nicolas, Choro Blanco, and Caballerisa intrusions and the Coymolache sill have similar $K_2O$ contents, ranging from 1.4 to 2.5 wt %. Samples from the Cerro Corona, Cerro Jesus, and Cerro San Jose intrusions contain variable $K_2O$ contents, up to 6.9 wt %, consistent with the presence of K-rich alteration minerals such as K-feldspar, biotite, and white mica. Most samples have low Th contents, <7 ppm, except samples Tanta-355 and Tanta-356 from the Tantahuatay area, with 11 and 10 ppm Th, respectively. All samples have bulk-rock Th/U ratios <5, except for sample CC5-s from Cerro Corona and sample Tanta-355, and all samples have low Nb contents, <8 ppm.

All bulk-rock samples contain moderate REE concentrations, with total REE ($\Sigma_{REE}$) ranging from 36 to 110 ppm, except for a low value (17 ppm) of the intensely altered sample 25-4 from the San Jose intrusion. All samples except for SG, CNG-1, Tanta-352, Tanta-355, Tanta-357, and Anta-6 have a moderately concave-upward chondrite-normalized REE pattern, with a negative slope from La to Yb ranging from 9 to 18 for $La_{cn}/Yb_{cn}$ (cn denotes the chondrite-normalized values) and nearly flat slope from Dy to Yb (1.1–1.4 $Dy_{cn}/Yb_{cn}$) (Fig. 7A). Younger rocks, such as the Hualgayoc rhyodacite and Tantahuatay igneous units, have lower $\Sigma_{REE}$ (83–54 ppm) than older intrusions (120–66 ppm). Samples SG, CNG-1, Tanta-352, Tanta-355, Tanta-357, and Anta-6 are intensely altered to residual quartz ± alunite ± pyrophyllite and have a pro-

nounced concave-upward REE pattern with lower contents of heavy REE (HREE), middle REE (MREE), and Y (1.3–0.5 ppm Dy, 0.5–0.3 ppm Yb, 5–2 ppm Y; Fig. 7B) than the least altered samples (Fig. 7A). The pronounced concave-upward REE pattern likely reflects the removal of HREE- and MREE-bearing minerals such as amphibole and probably ilmenite and apatite by acidic hydrothermal fluids, which can dissolve REE and Y (Fulignati et al., 1999; Van Dongen et al., 2010). Retention of minor light REE (LREE) in these rocks is explained by their incorporation into alteration minerals, such as alunite (Terakado and Fujitani, 1998). Sample 25-4 from the San Jose intrusion shows low LREE values, likely due to the lack of alunite to host LREE after dissolution by acidic fluids.

All bulk-rock samples (except those intensely altered) have negligible to weak positive and negative Eu anomalies ($Eu/Eu^* = [Eu_{cn}]/[(Sm_{cn}*Gd_{cn})^{0.5}]$), ranging from 0.7 to 1.1. Plagioclase preferentially incorporates $Eu^{2+}$ and its crystallization is the most common cause for Eu anomalies in igneous rocks. Samples from the Coymolache sill show weakly positive and weakly negative Eu anomalies, which likely reflect a minor difference in the abundance of plagioclase in samples.

### *5.2 U-Pb zircon ages*

U-Pb zircon ages were calculated from $^{206}Pb/^{238}U$ ratios (Table 2, Fig. 8), with most zircon grains producing concordant ages. A few outliers are due to inherent large analytical uncertainties of $^{207}Pb/^{235}U$ ratios because of a small fraction of $^{235}U$ and a short decay time to produce $^{207}Pb$ (Fig. A2-4, App. 2). Since the ages are for zircon rims, they represent the solidification of host igneous rocks. Inherited cores were only observed in the Cerro Corona Intrusive Complex, the Hualgayoc rhyodacite, and the PK porphyry dike (Fig. 6C). Two inherited cores of zircon dated from Cerro Corona yielded Cretaceous ages, indicating the incorporation of zircon grains from underlying Cretaceous sedimentary rocks (Fig. 1).

Our dating results indicate nearly continuous magmatism in the Hualgayoc district from 14.8 to 9.7 Ma (Fig. 8). U-Pb dates of zircon from intrusive phases 1, 4, 5, and 6 of the Cerro Corona Intrusive Complex (sample CC1; CC4 and CC4b; CC5 and CC5n; and CC6, respectively) yielded similar ages, from 14.59 ± 0.13 to 14.40 ± 0.12 Ma, with overlapping $2\sigma$ uncertainties (Table 2). Other magmatic activity contemporaneous with the Cerro Corona Intrusive Complex includes the San Jose, Cerro Jesus, Cerro Choro Blanco, Cerro Caballerisa, Cerro Las Gordas, San Miguel, and Cerro Cienaga intrusions, the PK porphyry dike, and the Coymolache sill. These intrusions all solidified between 14.83 ± 0.36 and 14.06 ± 0.49 Ma, with overlapping $2\sigma$ uncertainties, termed Group A (green symbols, Fig. 8). The San Nicolas intrusion was emplaced slightly later at 13.67 ± 0.28 Ma (sample SN). Igneous rocks hosting high-sulfidation Au mineralization at the Tantahuatay-2 zone of the Tantahuatay deposit (samples Tanta-352, 355, 356, and 357) were emplaced from 13.09 ± 0.27 to 12.46 ± 0.49 Ma. Subvolcanic intrusions and rhyolite dome of the Calipuy Formation in the Tantahuatay area yielded the ages of 13.18 ± 0.37 Ma (sample Anta-6), 12.01 ± 0.26 (sample Anta-PF), and 11.51 ± 0.37 Ma (sample Anta-8). These igneous rocks are Group B (red symbols, Fig. 8), including the San Nicolas intrusion. Finally, the Cerro Hualgayoc rhyodacite dome, north of the Cerro Corona deposit (Fig. 2), is the youngest igneous rock unit dated in the district, at 9.74 ± 0.31 Ma (Group C, blue symbol, Fig. 8).

### *Trace element composition of zircon*

Trace element compositions of all zircon grains (Table A2-3, App. 2) have similar chondrite-normalized REE patterns, with pronounced positive Ce anomalies and weak to moderate negative Eu anomalies (Eu/Eu*), ranging from 0.3 to 0.8 (Viala and Hattori, 2021). Zircon compositions in the district form two groups: older Group A intrusions (14.8–14 Ma) and younger Group B igneous rocks (13.7–11.5 Ma; Fig. 8). Group A includes zircon from the Cerro Corona, San Jose, Cerro Caballerisa, Cerro Choro Blanco, Anta-PF, San Miguel, and Cerro Las Gordas intrusions, and the Cerro Cienaga center of the Tantahuatay deposit. Zircons in Group A are characterized by a large range in the values of $\Sigma_{REE}$, from 170 to 1,000 ppm, and low Th/U, mostly between 0.5 and 0.1 (Fig. 9A). Zircon grains in Group A have a wide range of $\Sigma_{REE}$ content (180–1,100 ppm) and low Th/U ratios (mostly <0.5). Group B zircons from the Tantahuatay-2 center of the Tantahuatay deposit, the San Nicolas intrusion, and volcanic rocks of the Calipuy Formation are characterized by lower $\Sigma_{REE}$ contents, <550 ppm (Fig. 7C), and a wide range in Th/U ratios, between 1 and 0.2 (Fig. 9A).

### *Zircon crystallization temperatures*

Zircon crystallization temperatures were calculated using Ti-in-zircon geothermometry of Ferry and Watson (2007), assuming activities of $SiO_2$ ($a_{SiO_2}$) and $TiO_2$ ($a_{TiO_2}$) are 1 and 0.7, respectively. The value of 1 for $a_{SiO_2}$ is justified because of the presence of quartz phenocrysts. Activity of $TiO_2$ should be <1 since rutile was not observed to be an igneous mineral in our samples. Ilmenite microphenocrysts occur in several samples from the Cerro Corona, San Jose, and San Miguel intrusions, indicating that $a_{TiO_2}$ for these magmas was above 0.6 (Watson et al., 2006; Fu et al., 2008). We chose 0.7 for the $a_{TiO_2}$, which has been used for granitic to dioritic melt of similar bulk compositions and mineralogy (Chelle-Michou et al., 2014; Buret et al., 2016). Changing the values of $a_{TiO_2}$ by ±0.1 results in a minor difference in zircon crystallization temperature, ±15°C. The majority of Group A zircon grains yield crystallization temperatures of 710° to 640°C, with only minor decrease with increasing Hf content (Fig. 9D). Zircons from Group B show a wider range of crystallization temperatures, decreasing from 800° to 600°C with increasing Hf content (Fig. 9D).

### *Amphibole composition*

Most amphibole grains in igneous rocks in the study area show evidence of hydrothermal alteration. Four amphibole

Fig. 4. Simplified (A) geologic map covering the AntaKori deposit and the Tantahuatay-2 zone of the Tantahuatay deposits, provided by Regulus Resources Inc. (2021). Dashed red line shows the approximate areal extent of currently known high-sulfidation and skarn-style mineralization, projected to the surface. (B). Southwest-northeast cross section (section line in map). The PK porphyry dike is not represented in this figure and is associated with the Early Breccia.

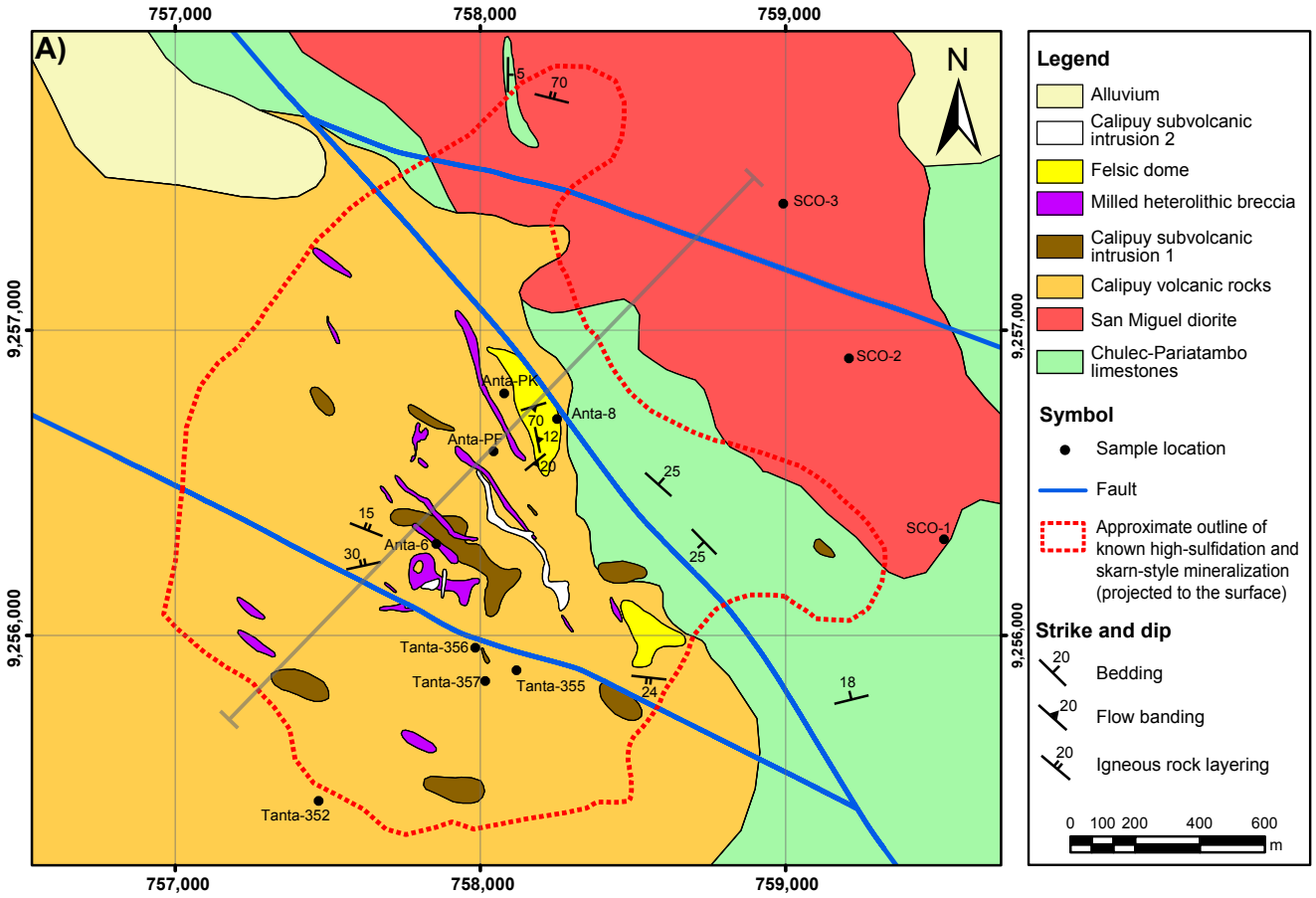
A)
757,000
758,000
759,000
9,257,000
9,256,000
N
SCO-3
SCO-2
SCO-1
Anta-PK
Anta-8
Anta-PP
Anta-6
Tanta-356
Tanta-357
Tanta-355
Tanta-352
5
70
70
12
20
25
15
30
25
24
18
Legend
Alluvium
Calipuy subvolcanic intrusion 2
Felsic dome
Milled heterolithic breccia
Calipuy subvolcanic intrusion 1
Calipuy volcanic rocks
San Miguel diorite
Chulec-Pariatambo limestones
Symbol
Sample location
Fault
Approximate outline of known high-sulfidation and skarn-style mineralization (projected to the surface)
Strike and dip
Bedding
Flow banding
Igneous rock layering
0 100 200 400 600
m

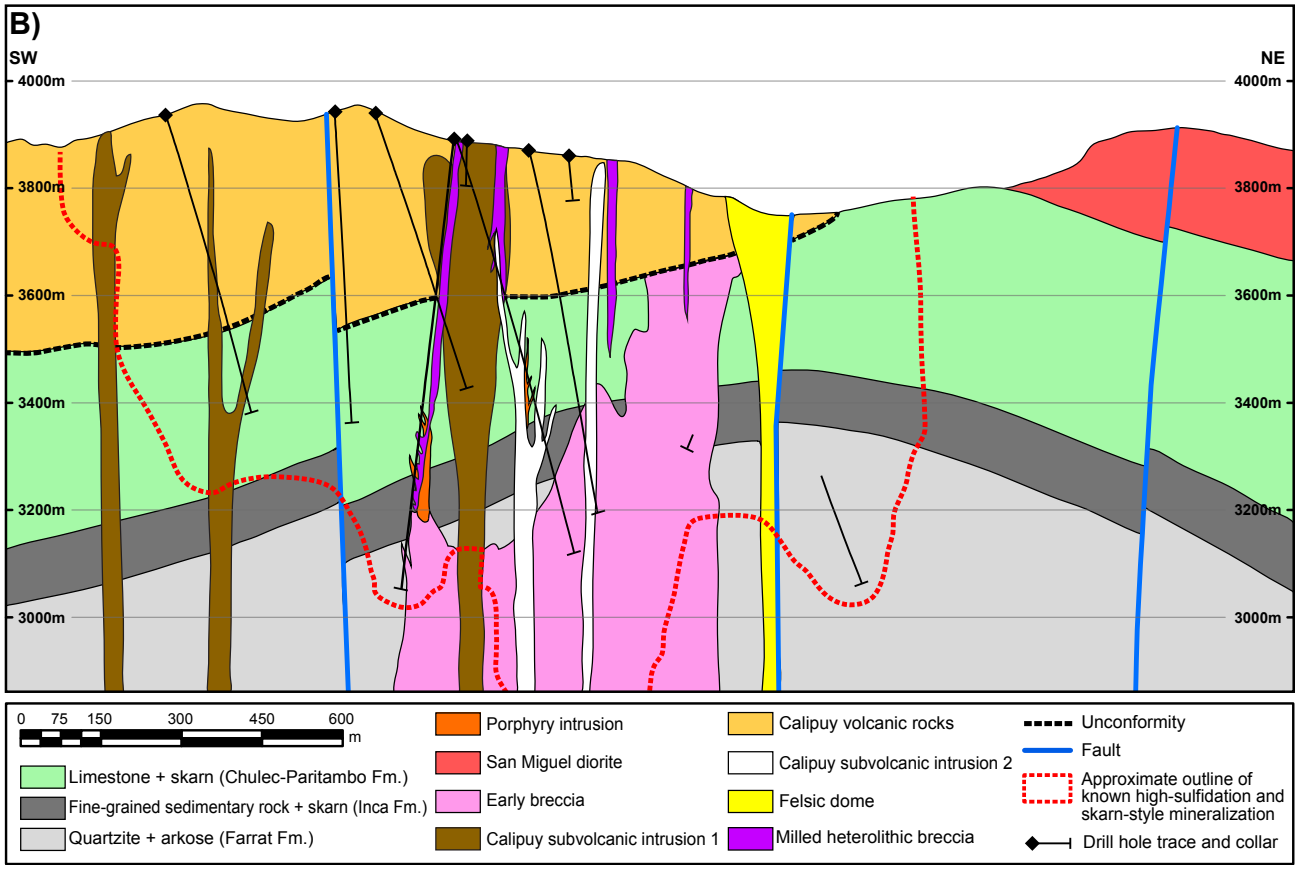
B)
SW
NE
4000m
3800m
3600m
3400m
3200m
3000m
0 75 150 300 450 600
m
Limestone + skarn (Chulec-Paritambo Fm.)
Fine-grained sedimentary rock + skarn (Inca Fm.)
Quartzite + arkose (Farrat Fm.)
Porphyry intrusion
San Miguel diorite
Early breccia
Calipuy subvolcanic intrusion 1
Calipuy volcanic rocks
Calipuy subvolcanic intrusion 2
Felsic dome
Milled heterolithic breccia
Unconformity
Fault
Approximate outline of known high-sulfidation and skarn-style mineralization
Drill hole trace and collar

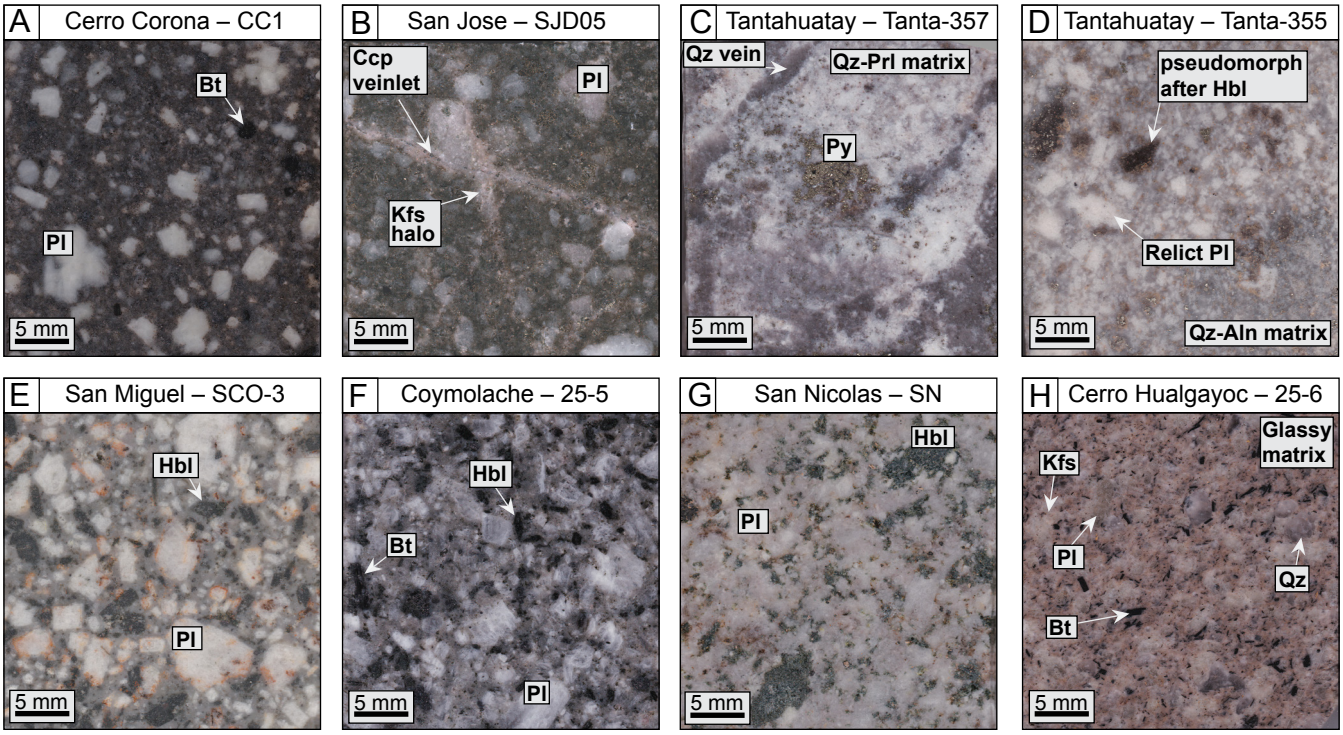


Fig. 5. Photographs of representative samples. (A). Sample CC-1 from phase 1 of the Cerro Corona Intrusive Complex. The sample contains primary biotite as well as secondary biotite after amphibole. (B). Sample SJD-05 from the San Jose intrusion, similar to sample CC-1 from the Cerro Corona Intrusive Complex, with secondary biotite in the matrix and chalcopyrite veinlets with alteration halo of light pink K-feldspar. (C, D). Samples Tanta-357 and Tanta-355, respectively, from the Tantahuatay Volcanic Complex. All primary minerals were replaced by quartz, pyrophyllite, and/or alunite. Sulfide minerals include pyrite and enargite disseminated and in quartz veins. (E). Sample SCO-3 from the San Miguel intrusion, with abundant amphibole phenocrysts, mostly replaced by chlorite. (F). Sample 25-5 from the Coymolache sill, with minor chloritization of biotite and amphibole phenocrysts. (G). Sample SN from the equigranular San Nicolas intrusion, with most amphibole crystals replaced by chlorite. (H). Sample 25-6 from the Hualgayoc rhyodacite dome, with phenocrysts of quartz, biotite, K-feldspar, and plagioclase in a glassy matrix, apparently unaltered. Abbreviations: Aln = alunite, Bt = biotite, Ccp = chalcopyrite, Hbl = hornblende, Kfs = potassic feldspar, Pl = plagioclase, Prl = pyrophyllite, Py = pyrite, Qz = quartz.

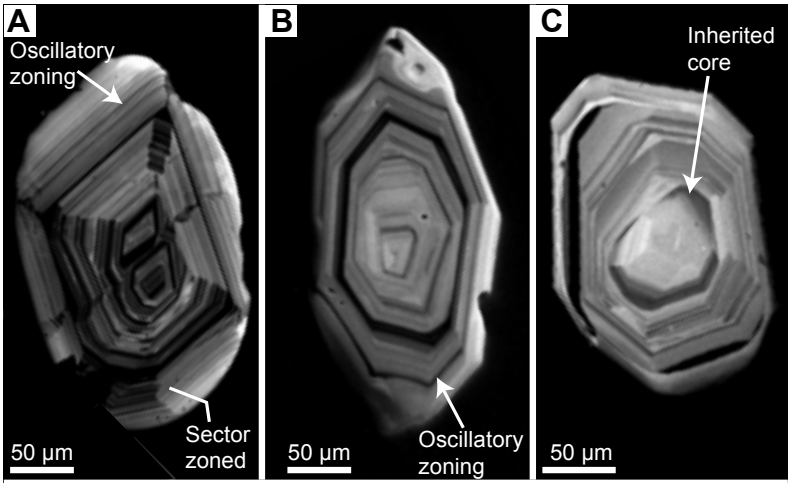


Fig. 6. Cathodoluminescence images of representative zircon grains. (A). Zircon from the San Miguel intrusion, with oscillatory and sector zoning (sample SCO-1). (B). Zircon from the Hualgayoc rhyodacite, with oscillatory zoning (sample 25-6). (C). Zircon from the AntaKori-Pk intrusion, with resorbed core of inherited zircon and coarse oscillatory-zoned overgrowth (sample Anta-PK).

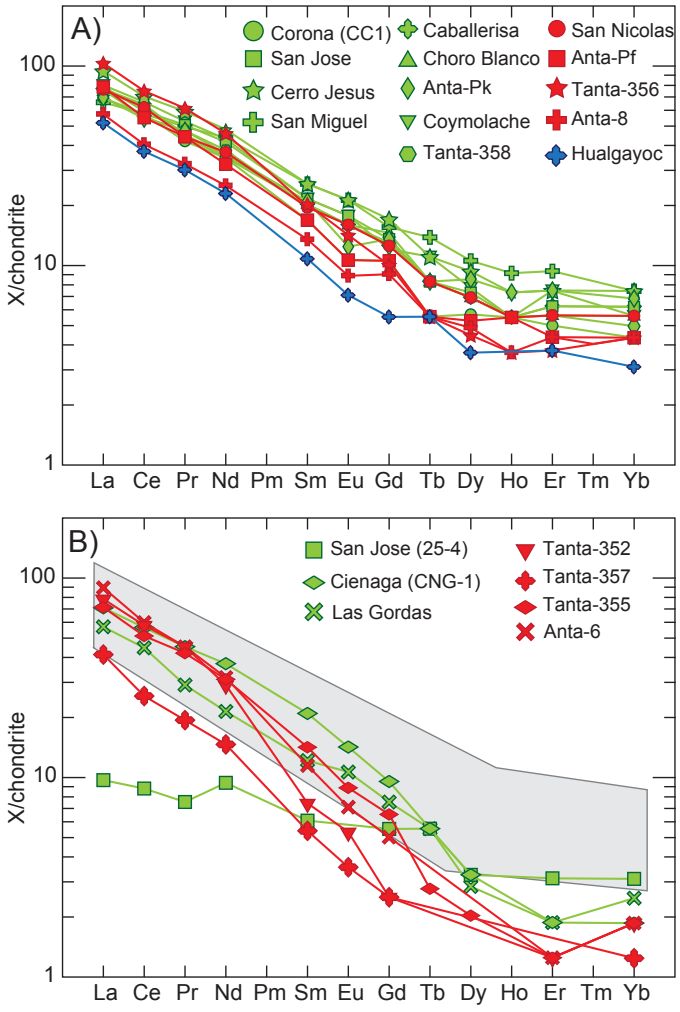


Fig. 7. Chondrite-normalized REE patterns of bulk-rock compositions of igneous rocks in the Hualgayoc district. Chondrite values are from McDonough and Sun (1995). (A). REE patterns of weakly to moderately altered samples. All samples show moderately concave-upward patterns with high LREE and relatively flat $Dy_{cn}$ to $Yb_{cn}$. (B). REE patterns of intensely altered samples. All samples have low values of MREE and HREE in contrast to less-altered samples. The weathered sample 25-4 from the San Jose intrusion also has low LREE values. Gray field corresponds to the range of values of least-altered samples. Colors are the same as in Figure 8, which distinguish the three age groups of igneous units in the district. All data obtained in this study.

phenocrysts from sample 25-5 of the Coymolache sill are euhedral to subeuhedral, moderately to strongly fractured, and contain inclusions of magnetite. Backscattered electron images show weak to moderate patchy alteration close to the rim and along fractures (Fig. A2-1, App. 2). The three amphibole phenocrysts from sample SN of the San Nicolas intrusion are subhedral to anhedral, moderately fractured, and have irregular alteration of chlorite (Fig. A2-2, App. 2). The compositions of unaltered areas of grains and different grains in individual samples from the Coymolache sill and San Nicolas intrusion have nearly identical composition (Table A2-7, App. 2), confirming that these grains retained primary igneous compositions. These amphibole compositions are magnesio-hornblende of the calcic amphibole group, following the nomenclature of Hawthorne et al. (2012). Amphibole from the Coymolache sill has an Mg# (=100*([Mg]/[Mg + $Fe_t$]) of 65–60, and $Al_2O_3$ content of 9.27 to 8.05 wt %. Amphibole from the San Nicolas intrusion has slightly higher Mg#, 75 to 76, and lower $Al_2O_3$ content, from 5.73 to 5.34 wt %.

These igneous amphibole grains are used to estimate the conditions of parental magmas during their crystallization. Empirical geothermobarometry, based on data of amphibole proposed by Ridolfi et al. (2010), yields temperatures from 862° to 830°C (±22°C $\sigma_{est}$) and a pressure from 191 to 139 Mpa (with ±20 Mpa maximum uncertainty) for the Coymolache sill, which corresponds to ~7- to 5-km depth, assuming a crustal density of 2.7 g/cm$^3$. Amphiboles from the San Nicolas intrusion crystallized at slightly lower temperature, 810° to 795°C (±22°C $\sigma_{est}$), and at lower pressures, of 77 to 70 Mpa (with ±8 MPa maximum uncertainty), which corresponds to ~3- to 2.5-km depth. Amphibole from the Coymolache sill records a parental magma oxygen fugacity of FMQ +1.5 to +2.0 (1.5–2 logarithmic units above the fayalite-magnetite-quartz redox buffer). Amphibole from the younger San Nicolas intrusion yields higher oxidation conditions, with values of about FMQ +3.0 (Fig. 10B), suggesting a slight increase in magmatic oxidation over time. Amphibole from the Coymolache sill yields a melt water content from 5.1 to 5.5 wt % $H_2O$ (±0.4 wt % $\sigma_{est}$), whereas amphibole from the San Nicolas intrusion records a water-in-melt content of ~2.8 to 2.9 wt % $H_2O$ (±0.4 wt % $\sigma_{est}$). Amphiboles from the San Nicolas intrusion plot slightly outside the stability limit of amphibole (Fig. 10C); however, considering analytical uncertainty, they likely crystallized close to their thermal stability limit. On the other hand, amphibole from the Coymolache sill plot well inside the stability field, consistent with the well-developed euhedral crystal habit of amphibole grains in the samples (Fig. A2-1, App. 2). Amphibole grains from the San Nicolas intrusion appear to have crystallized relatively late, based on the relatively low-temperature estimate (~800°C) and shallow crustal depth (~3 km; Fig. 10A).

## Discussion

### *Temporal evolution of magmatic-hydrothermal activity in the Hualgayoc district*

Macfarlane et al. (1994) suggested that magmatic activity in the Hualgayoc district began at 45 ± 3.4 Ma, in the Eocene, based on an Rb-Sr isochron age obtained from bulk-rock powder and mineral separates of a biotite-hornblende-quartz diorite collected at Cerro Coymolache. Since Rb and Sr are soluble in water, their abundances, especially for plagioclase and bulk-rock powder, are easily modified during subsolidus alteration. Recalculating the Rb-Sr isochron ages using the data presented by Mcfarlane et al. (1994) yielded varying isochron ages; 49 Ma from the biotite-bulk-rock pair and 27 Ma from plagioclase-hornblende pair. Therefore, we consider the true solidification age for the Coymolache sill is represented by our U-Pb zircon date of 14.52 ± 0.14 Ma (Table 2). The oldest unit we sampled in the study area is the Cerro Jesus intrusion, which has a U-Pb zircon age of 14.83 ± 0.36 Ma. Based on our data, magmatic activity in the district began in the middle Miocene.

Magmatic activity was widespread in the Hualgayoc district during the period of 14.8 and 14.0 Ma, with abundant intru-

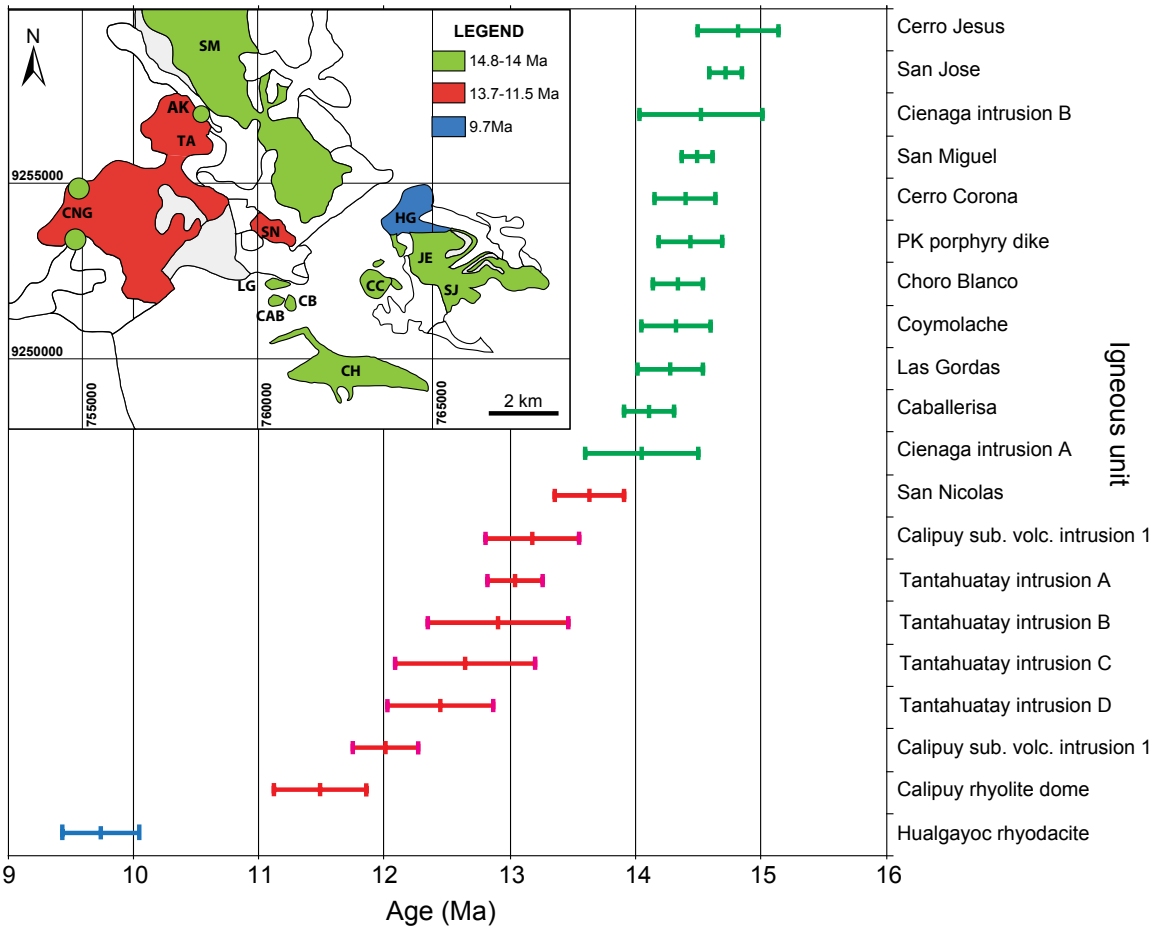


Fig. 8. $^{206}Pb/^{238}U$ zircon ages of igneous rocks in the Hualgayoc district, obtained in this study. Error bars represent $2\sigma$ uncertainties (Table 2). The ages derived from samples of the Cerro Corona Intrusive Complex include those of intrusive phases 1, 4, 5, and 6 (Table 2). The igneous units define three age groups: 14.8 to 14.0 Ma (green), 13.7 to 11.5 Ma (red), and 9.7 Ma (blue). The map insert shows the distribution of units of the three age groups in the Hualgayoc district.

sive activity (Group A, Fig. 8). Similar zircon ages of phases 1, 4, 5, and 6 of the Cerro Corona intrusive complex indicate successive intrusion over a short period at ~14.5 Ma. Macfarlane et al. (1994) reported a K-Ar age of 13.35 ± 0.27 Ma for hydrothermal biotite from an altered porphyry sample of Cerro Corona, which is about 1 m.y. younger than the U-Pb zircon ages of the intrusions obtained in this study. Considering the high temperature of potassic alteration, biotite formation is likely during the intrusive activity. Therefore, we consider that this young K-Ar age may be due to Ar loss from biotite as a result of heating by nearby intrusions.

The intense potassic and white-mica alteration of the San Jose, Cerro Jesus, and Cerro Corona intrusions (SJ, CJ and CC; Fig. 2) indicates that their parental magmas produced magmatic-hydrothermal activity. In contrast, the contemporaneous intrusions of San Miguel, Choro Blanco, and Caballerisa plus the Coymolache sill are only affected by weak to moderate chlorite + epidote alteration, indicating that little magmatic-hydrothermal activity was associated with these intrusions. The Cienaga intrusion and PK porphyry dike are proximal to the Tantahuatay Volcanic Complex and were affected by intense acidic hydrothermal alteration associated with the mineralization style of Tantahuatay.

Magmatic activity between 13.67 and 11.51 Ma (Group B) was focused in the western part of the district (red intrusions, inset map, Fig. 8). Intense magmatism occurred in the AntaKori area and the Tantahuatay-2 zone of the Tantahuatay deposit between ~13 and ~12 Ma, with eruption of the Calipuy Formation and emplacement of several subvolcanic intrusions (samples Anta-6, Anta-PF, Tanta-352, -355, -356 and -357; Fig. 8; Table 2). Magmatism was contemporaneous with the high-sulfidation epithermal Au mineralization at Tantahuatay, based on the similarity of our U-Pb zircon ages and $^{40}Ar/^{39}Ar$ ages of alunite at 12.4 ± 0.4 Ma (Noble and McKee, 1999), and 13.3 ± 0.06 to 11.01 ± 0.08 Ma for hypogene alunite and sericite (Prihar, 1998; Table A2.8, App. 2). The similarity of zircon and alteration mineral ages indicates that the dated igneous rocks are related to the causative intrusions responsible for forming the magmatic-hydrothermal systems that generated the mineral deposits.

The U-Pb zircon ages of rocks from the Cienaga zone of the Tantahuatay deposit (samples CNG-1 and Tanta-358) indicate magma solidification at 14.52 ± 0.49 and 14.06 ± 0.49 Ma, respectively, which are ~1 to 1.5 m.y prior to the ages of hypogene alunite, 13.3 to 11.01 Ma, reported by Prihar (1998) from the Tantahuatay deposit (Table A2.8, App. 2). The young

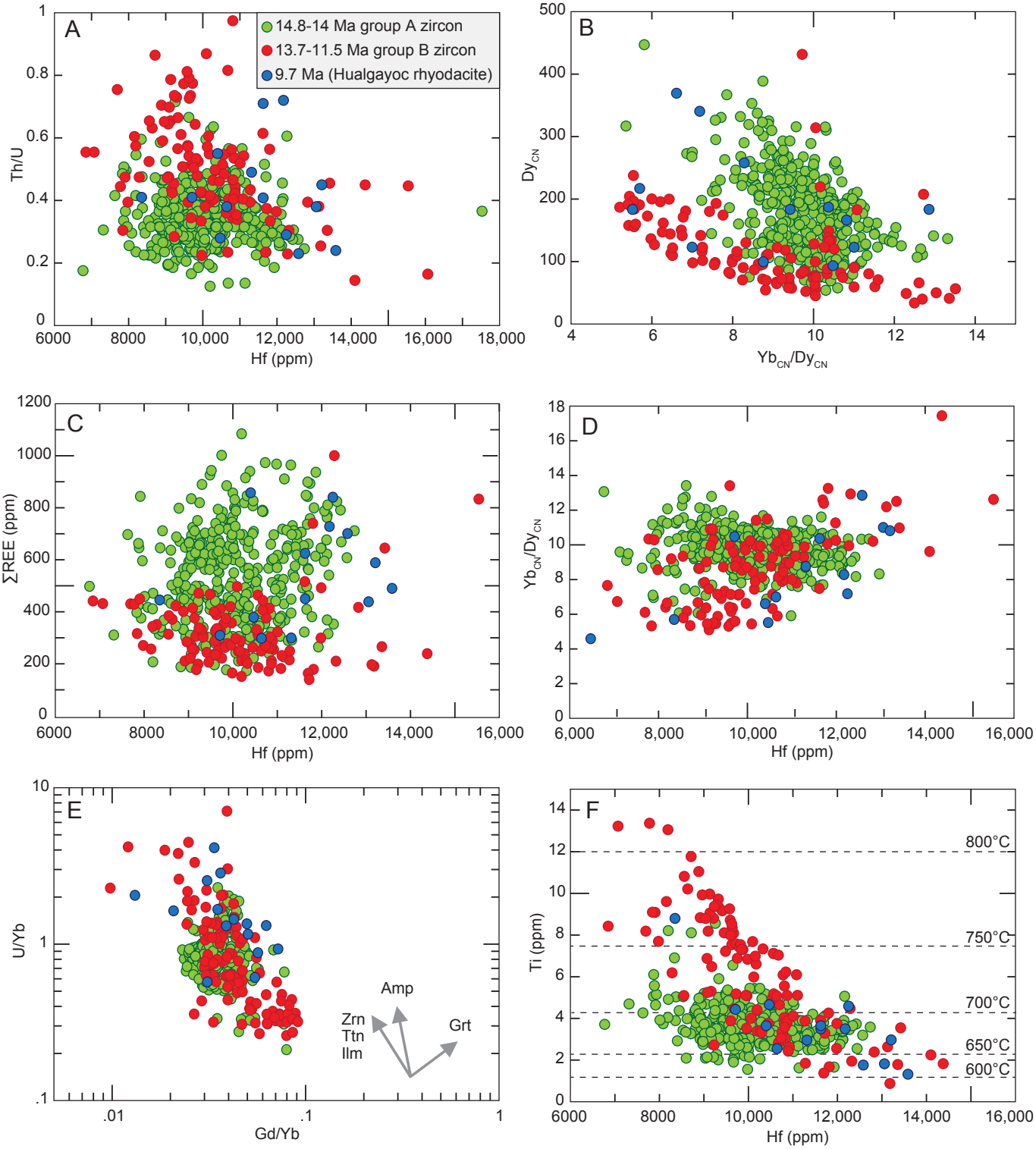


Fig. 9. Trace element composition of zircon ($n$ = 473) from the Hualgayoc district. Colors refer to the three age groups of igneous units (Fig. 8). The compositions of zircon from 14.8 to 14.0 Ma igneous rocks (Group A, green) are distinctly different from those of 13.7 to 11.5 Ma igneous rocks (Group B, red). Zircons of the Hualgayoc rhyodacite (9.74 ± 0.31 Ma) in blue. The general trends due to accessory mineral fractionation in (E) are from Grimes et al. (2015). Temperature values in (F) refer to zircon crystallization temperatures, using Ti contents in zircon, calculated with the method of Ferry and Watson (2007), assuming $a_{SiO_2}$ = 1 and $a_{TiO_2}$ = 0.7.

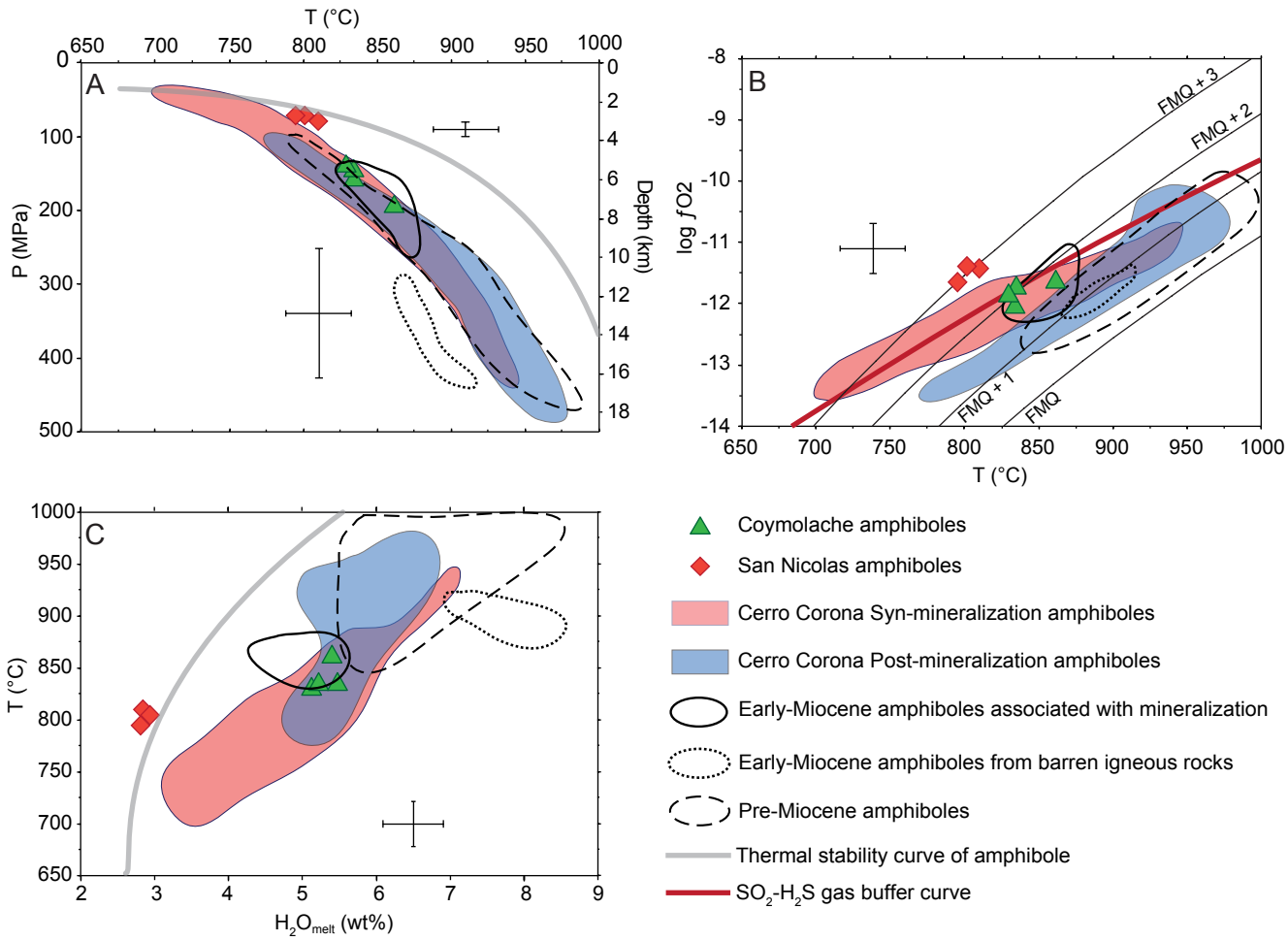


Fig. 10. Pressure, temperature, $f_{O_2}$ and $H_2O$ content of melt, based on the amphibole composition from Coymolache sill ($n$ = 4), San Nicolas intrusion ($n$ = 3), the Cerro Corona Intrusive Complex ($n$ = 34), pre-Miocene igneous rocks (57–29.5 Ma; $n$ = 26), and early to middle Miocene (23–16 Ma) igneous rocks ($n$ = 16) in the Cajamarca region, based on geothermobarometry of Ridolfi et al. (2010). Upper thermal stability of amphibole is shown by the solid gray curve in (A) and (C). (A). Error bars represent the standard error of estimates for temperature and pressure. The depth and maximum depth uncertainties (larger at greater depth) are calculated using rock density of 2.7 g/cm$^3$. (B). FMQ, and FMQ +1 to +3 buffer curves shown by solid black curves. The red line represents the $SO_2$-$H_2S$ gas buffer curve of Einaudi et al. (2003). Error bars represent the maximum uncertainty of log $f_{O_2}$ and the standard error of estimate for temperature. (C). Error bars represent the standard error estimate of temperature and $H_2O_{melt}$. The data for the Cerro Corona Igneous Complex are from the unpublished PhD thesis of Longridge (2016), who used the same geothermobarometry as this study. The values for pre-, early, and middle Miocene rocks were calculated from amphibole compositions reported in the unpublished PhD thesis of Davies (2002).

$^{40}Ar/^{39}Ar$ ages of alunite together with the U-Pb zircon age of rhyolite dome of the Calipuy Formation (sample Anta-8), at 11.51 ± 0.37 Ma, suggest that the hydrothermal activity likely persisted until 11.01 ± 0.08 Ma (alunite $^{40}Ar/^{39}Ar$ age; Prihar, 1998).

After a ~1.5-m.y. hiatus in magmatic activity in the district, the barren Cerro Hualgayoc rhyodacite dome intruded north of the Cerro Corona deposit at 9.74 ± 0.31 Ma (sample 25-6, blue, Fig. 8). This magmatism was followed by eruption of rhyodacite tuff and emplacement of rhyodacite domes and dacite dikes in the Tantahuatay area at 9.59 ± 0.06 to 8.31 ± 0.03 Ma, based on $^{40}Ar/^{39}Ar$ ages of magmatic biotite and sanidine (Macfarlane et al., 1994; Prihar, 1998; Noble and Mckee, 1999; Table A2.8, App. 2). These dates record the latest magmatism and magmatic-hydrothermal activity in the Hualgayoc district.

*Magma source and evolution in the Hualgayoc district*

Bulk-rock compositions of igneous rocks in the Hualgayoc district show low concentrations of MREE and HREE and a moderate concave-upward chrondrite-normalized REE pattern (Fig. 7A). Overall low concentrations of MREE and HREE suggest effects of amphibole and garnet on the melt composition. Among the two minerals, amphibole likely played the major role in controlling the abundances of REE due to low concentrations of MREE relative to HREE. Amphibole preferentially incorporates MREE over HREE (Sisson, 1994; Tiepolo et al., 2007). Partition coefficients (D) between amphibole and melt for La, Dy, and Yb in andesitic melt are ~0.5, 4.4, and 2.7 respectively (Sisson, 1994). We suggest that amphibole plus minor garnet as residues in the magma sources produced low MREE in the parental magmas in the Hual-

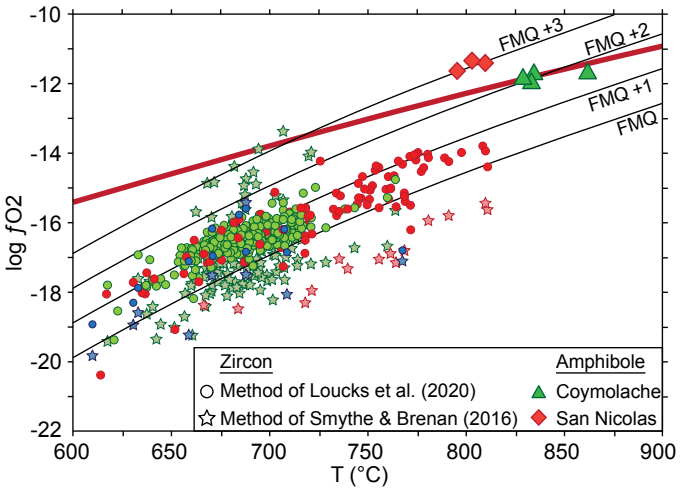


Fig. 11. Magma $f_{O_2}$ values from zircon composition using the method of Loucks et al. (2020) and Smythe and Brenan (2016), and those obtained from amphibole compositions. Zircon crystallization temperatures from Figure 9D. Buffer curves shown for FMQ and FMQ +1 to +3. Standard errors for the method of Loucks et al. (2020) are ±0.6 log $f_{O_2}$, and ±1 log $f_{O_2}$ for the method of Smythe and Brenan (2016). The red line represents the $SO_2$-$H_2S$ gas buffer curve. Colors as in Figure 8.

gayoc district. Subsequent fractional crystallization of amphibole resulted in further lowering of MREE relative to HREE.

Igneous rocks with ages of 14.8 to 14.0 Ma (green, Fig. 8) are dioritic in composition, with similar mineralogy. By contrast, younger rocks, formed between 13.7 and 9.7 Ma, such as the rhyolite dome of the Calipuy Formation and the Hualgayoc rhyodacite dome, are more felsic. Not only major element abundances, but also minor and trace element concentrations show temporal changes. Relatively unaltered igneous rocks in the district show a steady decrease in the concentrations of V and $\Sigma_{REE}$, and a slight increase in $La_{cn}/Yb_{cn}$ ratios, from 9 to 17, with decreasing ages from 14.8 to 9.7 Ma. The temporal change in bulk-rock composition may be explained by (1) increasing fractional crystallization of amphibole in the melt (2), increasing abundance of residual garnet at the source, (3) progressive assimilation of crustal rocks, or (4) smaller degrees of partial melting at the source of younger rocks.

Possibilities (1) and (2) are likely. Possibility (1) is consistent with abundant occurrences of amphibole phenocryst in most rocks. Fractional crystallization of amphibole also explains lower Mg contents in younger rocks. Possibility (2) likely had a very minor role. Garnet has larger D values for HREE than MREE and a partial melt formed from the sources with garnet residue would have $Dy_{cn}/Yb_{cn} >> 1$. Relatively unaltered igneous rocks in the Hualgayoc district show a small change in $Dy_{cn}/Yb_{cn}$: <1.5 for older rocks and <1.3 for younger rocks. Therefore, we suggest that fractional crystallization of amphibole was the major control on the change in the magma composition over time in the Hualgayoc district.

Possibility (3) assimilation of crustal material appears minimal, based on low Th contents in bulk-rock compositions and bulk-rock Sr isotope data (Macfarlane, 1989; Macfarlane et al., 1994). This is further supported by rare inherited zircon observed during this study. Possibility (4) decreasing degree of partial melting at the source would produce melt with increasing incompatible elements. A decrease in $\Sigma_{REE}$ in younger rocks is not consistent with the decreasing degrees of partial melting.

*Evolution of magma recorded by zircon composition*

The composition of zircon reflects that of the melt at the time of its crystallization. Zircon composition shows a distinct difference among three age groups (Group A, 14.8–14.0 Ma; Group B, 13.7–11.5 Ma; Group C, 9.8 Ma; Fig. 9). Bulk-rock compositions record gradual changes, but they do not show a sharp change among these rock groups (Fig. 7). Therefore, the difference in zircon composition is attributed to cocrystallizing phases.

Minerals cocrystallizing with zircon in our samples are evaluated based on their D values of REE. When a mineral with high D values of elements crystallizes, the melt will have lower concentrations of these elements. Titanite crystallization lowers MREE in a melt due to high D values compared to those for LREE and HREE; the values for La, Dy, and Yb are 113, 935, and 393, respectively (Bachmann et al., 2005). Titanite crystallization causes an increase in Eu/Eu* in the melt because of its slightly greater affinity for Sm and Gd over $Eu^{3+}$ (Bachmann et al., 2005; Loader et al., 2017). Amphibole crystallization has a similar effect as titanite but to a lesser degree, due to moderate D values for REE (<10 for all REE; Sisson, 1994) compared to those for titanite. Plagioclase crystallization causes a decrease in Eu/Eu* in the melt due to high D for $Eu^{2+}$ (Dunn and Sen, 1994). Apatite crystallization lowers the concentrations of LREE and MREE in a melt due to high D values (~10; Prowatke and Klemme, 2006).

The $Yb_{cn}/Dy_{cn}$ ratios of zircon in Groups B and C increase with decreasing $Dy_{cn}$ and increasing Hf (red and blue symbols, Fig. 9B, D). The increase in $Yb_{cn}/Dy_{cn}$ is also accompanied by a slight increase in Eu/Eu* in zircon, from ~0.4 to ~0.8. Moreover, zircon grains of Groups B and C show a significant increase in Yb/U ratios with decreasing Gd/Yb ratios, and those in Group B have low $\Sigma_{REE}$ content (<550 ppm, red symbols, Fig. 9C). This is consistent with cocrystallization of minor amount of titanite with zircon in magmas in Groups B and C. This is supported by the occurrence of titanite pseudomorphs replaced by aggregates of rutile in sample Anta-PF from the Calipuy subvolcanic intrusion 1. In contrast, zircon grains from Group A have higher contents of $\Sigma_{REE}$ and Dy than Group B zircon grains, and do not show a clear relationship between $Dy_{cn}$ and $Yb_{cn}/Dy_{cn}$ ratios (green symbols, Fig. 9B). In addition, $Yb_{cn}/Dy_{cn}$ appears to decrease slightly with increasing Hf (Fig 9D). These observations indicate that titanite did not crystallize before and during zircon crystallization in magmas of Group A. Group A zircon grains are characterized by relatively cool crystallization temperatures, between 720° and 640°C for most grains (green symbols, Fig. 9F), independent of Hf concentrations. The data suggest that the parental magmas solidified at relatively constant temperature, and distinctly cooler than those for most Group B zircon grains. By contrast, Group B zircon grains record a larger decrease in crystallization temperatures, from ~800° to ~620°C with increasing Hf content (red symbols, Fig. 9F), indicating that the magmas were saturated with zircon at high temperatures and zircon growth continued during the solidification of the magmas. Zircon crystallization temperatures of Group A are lower than zircon saturation temperatures rang-

ing between 775° and 700°C (Fig. 12) obtained using bulk-rock compositions (Watson and Harrison, 1983).

Due to the intense alteration of most samples of Group B zircon, the zircon saturation temperature from bulk-rock composition was not calculated, except for the unaltered sample SN from the San Nicolas intrusion, which yields a zircon saturation temperature of 720°C, similar to most samples of Group A zircon (Fig. 12). Zircon grains from the sample show a wide range of zircon crystallization temperatures, from ~810° to ~670°C, with three quarters of grains showing higher crystallization temperature than the zircon saturation temperature of 720°C. The discrepancy of these values may be attributed to underestimation of $a_{TiO_2}$, which is assumed to be 0.7 for the calculation of zircon crystallization temperatures. However, an increase in $a_{TiO_2}$ from 0.7 to 1 only decreases the calculated temperature by about 35°C, insufficient to explain the high crystallization temperatures of half of the zircon grains from the sample. Hydrothermal alteration is unlikely to have been the cause of the discrepancy observed in sample SN, as it is affected by very weak chloritization. We suggest that several zircon grains may have crystallized in a hot melt, different from the parental magma of the host rock, and were later incorporated into the cooler parental magma. Since zircon would not dissolve in a cooler magma, these zircon grains retained their original composition and high Ti. The interpretation is consistent with the morphology of zircon grains from sample SN, most being subhedral in shape, and just a few euhedral grains with sharp crystal faces (Sample SN, App. 2, Fig. A2-3).

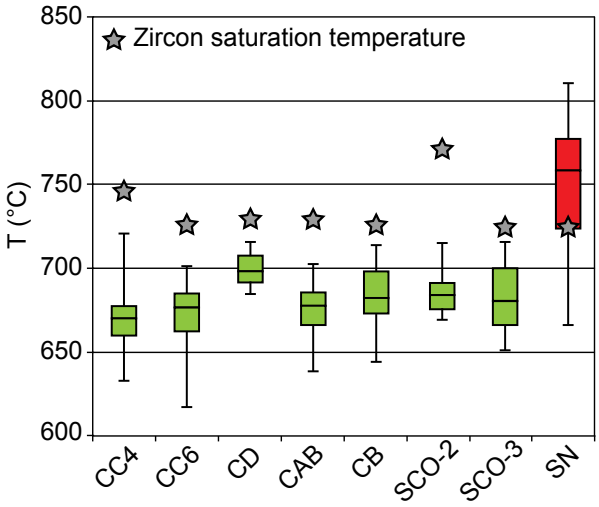


Fig. 12. Zircon crystallization temperature of weakly to moderately altered samples, shown as box-whisker plots (upper and lower quartile values, and entire range), compared to zircon saturation temperatures (gray stars) from intrusions in the Hualgayoc district. CC4 and CC6 = Cerro Corona phase 4 and 6, respectively; CD = Coymolache sill; CAB = Caballerisa; CB = Choro Blanco; SCO2 and SCO3 = San Miguel; SN = San Nicolas. Colors as in Figure 8. Zircon saturation temperatures were calculated by the method of Watson and Harrison (1983).

### *Characteristics of Hualgayoc magmas based on amphibole composition*

Crystallization of amphibole in intermediate composition magma requires relatively high $H_2O$ contents (≥3–4 wt %; Naney, 1983; Ridolfi et al., 2010). This is consistent with the estimated melt water contents of ~3 wt % for the barren San Nicolas intrusion and >5 wt % for the barren Coymolache sill (Fig. 10C), based on the empirical relationship between amphibole composition and melt water content (Ridolfi et al., 2010). These high-water contents suggest that the parental magmas of the two barren intrusions were close to or saturated with water during the crystallization of amphibole phenocrysts at a depth of ~7 km for the Coymolache sill and ~3 km for the San Nicolas intrusion. Longridge (2016) obtained melt water contents from 3 to 6 wt % for the Cerro Corona Intrusive Complex based on amphibole composition, using the geothermobarometer of Ridolfi et al. (2010).

Our data compilation (Fig. 10C) shows that melt water contents decreased at lower temperatures and lower pressures, suggesting that magmas released aqueous fluids during cooling and ascent, and these fluids likely contributed to the magmatic-hydrothermal activity responsible for mineralization in the district. The compositions of amphibole phenocrysts from postmineralization dikes in the Cerro Corona Intrusive Complex also yield a high-water content in the melt (4.5–7 wt %) and high crystallization temperature (775°–975°C), indicating that postmineralization dikes also formed from hot, hydrous magma. These results suggest that all magmas in the Hualgayoc district were water rich, at or close to water saturation during hornblende crystallization, regardless of whether or not they were associated with porphyry- or epithermal-style mineralization.

Amphibole from synmineralization intrusions of the Cerro Corona Intrusive Complex record an increase in oxidation state during cooling, from FMQ +1 at 950°C to slightly above FMQ +3 at about 700°C. This change is parallel to the $SO_2$-$H_2S$ gas buffer curve (red field, Fig. 10B), similar to the S gas buffer reflection of (influence on) magma oxidation conditions noted by Einaudi et al. (2003) for intrusive rocks of other regions. Amphiboles from postmineralization dikes of the Cerro Corona Intrusive Complex (blue field, Fig. 10B) record a similar oxidation state as that of synmineralization intrusions at high temperature, although oxidation conditions approximated the rock buffer curve (Einaudi et al., 2003) at ~FMQ +1 during cooling. This means that the crystallized post-mineralization intrusions had a lower oxidation state compared to syn-mineralization crystallized intrusion at Cerro Corona (Fig. 10B). Amphibole compositions from the Coymolache sill and San Nicolas intrusion, both apparently barren, indicate a high oxidation state, about FMQ +2 and FQM +3, respectively (Fig. 10B), similar to and higher than the oxidation state of synmineralization intrusions of the Cerro Corona intrusive complex.

### *Magma oxidation conditions indicated by zircon*

We determined the oxidation condition of magmas using zircon oxibarometery. A variety of zircon oxibarometers have been proposed (e.g., Trail et al., 2012). We chose to use recently proposed oxibarometers of Smythe and Brenan (2016) and Loucks et al. (2020), since both are empirically proposed, based on many igneous rock samples. The zircon oxibarometer of Smythe and Brenan (2016) requires the parental melt composition and water content at the time of zircon crystallization. We used bulk-rock compositions as proxies for melt

compositions and the values of LOI as proxies for melt water content, as our samples contain no carbonate and little sulfides. The $f_{O_2}$ was calculated on a hydrous basis, similar to the method employed by Kobylinski et al. (2020) for host igneous rocks of the Gibraltar porphyry Cu-Mo deposit. Values of $f_{O_2}$ calculated on an anhydrous basis, as recommended by Smythe and Brenan (2016), yielded unrealistically low $f_{O_2}$ values, far below FMQ, for all samples. The $f_{O_2}$ values calculated from zircon using this modified method of Smythe and Brenan (2016) returned a wide range, from ~FMQ –1 up to FMQ +3, although most zircon yielded values from FMQ –1 to FMQ +1 (Fig. 11; star symbols). Since the zircon oxibarometer of Smythe and Brenan (2016) is sensitive to water content in the melt, weakly altered samples with LOI from 1.51 to 6.28 wt % were used for the calculations. The samples still yielded a wide range in $f_{O_2}$ values.

The zircon oxibarometer of Loucks et al. (2020), also based on empirical observations, only uses the trace element abundances of zircon. Most zircon grains yield slightly higher, less dispersed $f_{O_2}$ values than those obtained using the method of Smythe and Brenan (2016), with most values in the range of FMQ and FMQ +1.5 (Fig. 11; circle symbols); there is no apparent variation with decreasing crystallization temperatures.

Both zircon oxibarometers yield significantly lower $f_{O_2}$ values than the values commonly considered for magmas associated with porphyry systems, >FMQ +1.5. Nearly all of our $f_{O_2}$ values based on zircon composition plot below the $SO_2$-$H_2S$ gas buffer curve, whereases values based on amphibole composition from the mineralized Cerro Corona and barren San Nicolas intrusion and Coymolache sill broadly follow the buffer curve (Fig. 10B).

Most rocks contain quartz, magnetite, and magnesian amphibole (Mg# >65) in the Hualgayoc district. In addition, titanite was likely present in several samples based on the presence of pseudomorphs and it is consistent with the compositional variation for Group B zircon grains (Fig. 9E). The assemblage of quartz + titanite + magnetite + magnesian amphibole (Mg # >65) suggest that the magmas had high $f_{O_2}$, above FMQ +2 (Wones, 1989; Kohn, 2017). The $f_{O_2}$ values are comparable to the estimates based on amphibole compositions. Our study suggests that zircon oxibarometry yields unrealistically low $f_{O_2}$ values.

### *Comparison of the Hualgayoc district with igneous rocks in the Cajamarca region*

Pre-Miocene igneous rocks in the Cajamarca region are barren and primarily composed of plagioclase, amphibole, and pyroxene without biotite. The bulk-rock compositions are characterized by higher concentrations of compatible elements compared to Miocene rocks (Davies, 2002). The change from pre-Miocene to Miocene magmatism is reflected by lower concentrations of Yb and higher ratios of La/Yb (Fig. 13A) in Miocene rocks.

Miocene igneous rocks in the Cajamarca region formed in response to the subduction of the Nazca plate below the South American plate. They include early Miocene intrusions (23–16 Ma) associated with the Michiquillay, El Galeno, and Perol porphyry Cu-Au deposits and contemporaneous barren intrusions, and late Miocene (14.5–8.4 Ma; Longo et al., 2010) igneous rocks from the high-sulfidation Au deposits in the Yanacocha district (Fig. 1). Miocene intrusions are dioritic to granodioritic and contain amphibole ± biotite phenocrysts, whereas volcanic rocks are andesite to rhyolite with phenocrysts of amphibole ± biotite ± clinopyroxene ± K-feldspar (Chiaradia et al., 2009; Longo et al., 2010). All Miocene igneous rocks in the Cajamarca region are similar in lithology, mineralogy, and bulk-rock composition to those in the Hualgayoc district, suggesting a similar origin of the parental magmas. The abundant amphibole in most rocks in the region confirms the hydrous nature of the magmas.

All Miocene igneous rocks in the Cajamarca region contain between 58 and 70 wt % $SiO_2$, low MgO (<4 wt %), low $TiO_2$ (<0.7 wt %), and low compatible elements, such as Ni and Cr, compared to pre-Miocene rocks (Davies 2002; Chiaradia et al., 2009). Mineralized early Miocene intrusions in the Cajamarca region have slightly higher $SiO_2$, >63 wt %, than most

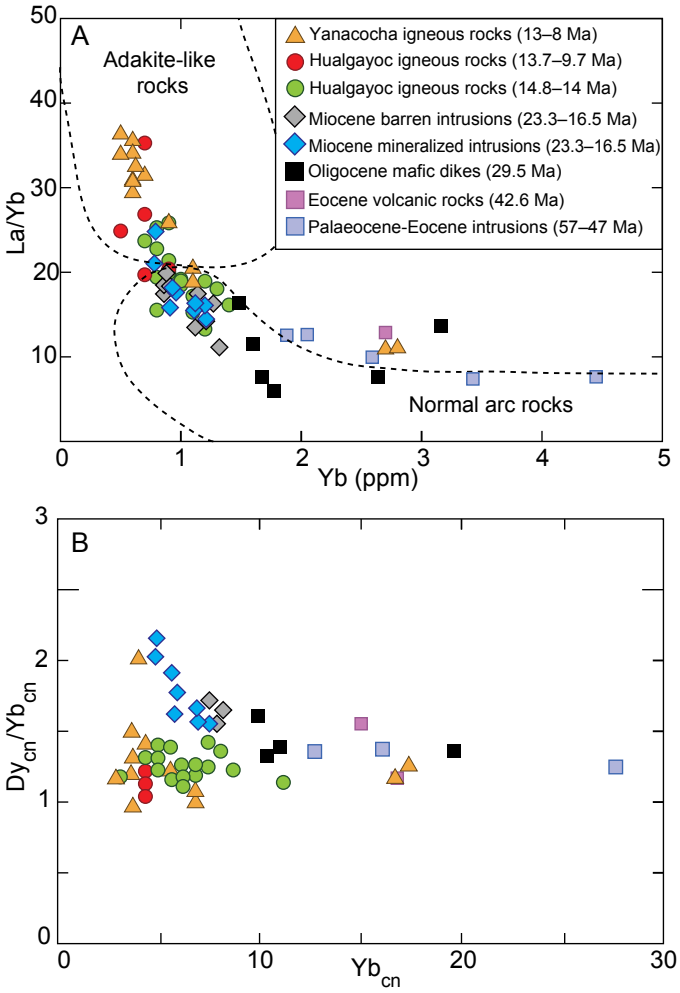


Fig. 13. Whole-rock compositions of igneous rocks from the Cajamarca region. (A) La/Yb vs. Yb (ppm) and (B) $Dy_{cn}/Yb_{cn}$ vs. $Yb_{cn}$ of pre-, early, and middle to late Miocene ages from the Yanacocha and Hualgayoc districts. Fields for adakite-like and normal arc rocks from Richards and Kerrich (2007). Data from pre- and early Miocene igneous rocks in the Cajamarca area are from Davies (2002); data from Yanacocha igneous rocks are from Chiaradia et al. (2009). The values $Dy_{cn}$ for pre- and early Miocene rocks were calculated using the abundances of Tb and Ho.

barren intrusions of similar age from the Hualgayoc district. All have low HREE, with Yb <1.6 ppm and high La/Yb, ranging from 13 to 37 (Fig. 13A).

Early Miocene intrusions in the region have a nearly straight, negatively sloped normalized pattern of REE, with minimal MREE depletion relative to HREE ($Dy_{cn}/Yb_{cn}$ ranging from 1.6–2.2). In contrast, igneous rocks in the Yanacocha and Hualgayoc districts show a concave-upward chondrite-normalized REE pattern with $Dy_{cn}/Yb_{cn}$ ranging from 1 to 1.5, except for one sample from the Yanacocha district with a value of 2 (Fig. 13B). The data suggest greater degrees of amphibole crystallization in middle to late Miocene magmas of the Hualgayoc and Yanacocha districts compared to early Miocene magmas. There is an overall increase in La/Yb ratios with decreasing Yb over time in all rocks in the Cajamarca region (Fig. 13A), reflecting depletion of HREE in magma with time. Older igneous rocks (14.8–13.7 Ma) in the Hualgayoc district have La/Yb ratio similar to early Miocene intrusions, <35, with most plotting in the normal arc rock field (Fig. 13B), whereas younger igneous rocks in the Hualgayoc district (13.7–9.7 Ma) have higher La/Yb ratio, above 20, plotting within the adakite-like compositional field (Richards and Kerrich, 2007), similar to those of igneous rocks from the Yanacocha district (Fig. 13B). This change in REE abundances suggests that garnet may have started to appear in the source at the time of younger magmatic activity in the Hualgayoc district. The increasing crust thickness during the Quechua orogeny, starting at 17 Ma, may have promoted crystallization of garnet at depth in the area (Chiaradia et al., 2009; Longo et al., 2010).

### *Characteristics of mineralized and barren igneous rocks*

Magmas associated with large porphyry-style mineralization are oxidized and water rich (Ishihara, 1977; Richards, 2014), ~FMQ +2 (Wang et al., 2014; Hattori, 2018). Data from the Hualgayoc district indicate that all magmas were oxidized (>FMQ, up to FMQ +3) and water rich (≥3 wt % $H_2O$), regardless of the association of mineralization with the intrusions. Therefore, these potentially fertile magmas must have had additional factors to favor mineralization.

The depth of emplacement is an important factor in the generation of magmatic fluids, since the solubility of water in a magma decreases sharply at depths <5 km (Moore et al., 1995). Ascent to this depth commonly results in saturation and exsolution of magmatic aqueous fluids. High-sulfidation epithermal deposits, such as at Tantahuatay, form at <500 to 1,000 m below the surface (Sillitoe and Hedenquist, 2003), as the shallow part of a mineralized porphyry system (Arribas et al., 1995; Hedenquist et al., 1998; Sillitoe, 2010). In the Hualgayoc district there are several Miocene faults (Benavides-Cáceres, 1999) trending northwest-southeast and northeast-southwest (Fig. 2), which separate rocks of the Tantahuatay Volcanic Complex from other intrusions located to the east. Considering the Tantahuatay Volcanic Complex formed at shallow depths, the eastern and southern parts of the study area likely now expose deeper levels of the upper crust. It is possible that the 14.5 Ma Cerro Corona porphyry deposit may have been accompanied by high-sulfidation mineralization at a shallower level, but it has since been eroded away. Equally, porphyry-style mineralization may be present at depth below the Tantahuatay deposit, as supported by breccia fragments of porphyry rocks with potassic alteration.

The shape and mode of occurrence of the intrusion are two additional, morphological features that are considered to influence the formation of a porphyry deposit (Sillitoe, 2010). Narrow, cylindrical phases of the Cerro Corona Intrusive Complex allowed magmatic-hydrothermal activity to be focused in a localized area, leading to the precipitation of metals at a high concentration to generate economic mineralization. In contrast, sills such the Coymolache sill, and relatively small single-phase intrusions such as Choro Blanco and Caballerisa, appear not to have been associated with appreciable magmatic hydrothermal activity, as evidenced by the lack of significant hydrothermal alteration of these intrusions. This also applies to the San Miguel diorite, which covers a large surface area in the district (Figs. 2, 4), but the unit appears to be a thin sheet, based on recent drilling results (Kevin Heather, pers. commun., 2021). Similar to the Hualgayoc district, the porphyry-type deposits in the Cajamarca regions are older, formed at 22 to 14 Ma, and more deeply eroded to be exposed, whereas the Yanacocha high-sulfidation deposits are younger, 13 to 8 Ma. The exception is the porphyry Cu-Au mineralization at Kupfertal and contemporaneous high sulfidation Au deposit at San Jose Sur, both of which formed at 10.78 Ma (Longo et al., 2010). High-sulfidation Au deposits in the proximal area including San Jose, Corimayo, and Punta Negra deposits formed slightly after the Kupfertal mineralization (Longo et al., 2010).

Pre-Miocene and Miocene intrusions in the Cajamarca region had a high oxidation state, above FMQ and were water rich, >4 wt % $H_2O$ (Fig. 10B, C). Despite the oxidized and hydrous nature of the pre-Miocene magmas, they are apparently not associated with mineralization, unlike Miocene-age intrusions. These observations support our conclusion that other factors are also required to form a mineral deposit.

## Conclusions

Detailed U-Pb dating of zircon from intrusions in the Hualgayoc district indicates that magmatism occurred continuously during the Miocene period, from 14.8 to 9.7 Ma. Rocks with the ages from 14.8 to 14.0 Ma are mostly in the eastern part of the Hualgayoc district and those from 13.7 to 11.5 Ma in the western part. The Cerro Corona porphyry Au-Cu deposit in the eastern part formed at ~14.5 Ma, contemporaneous with barren intrusions and sills of similar mineralogy. Volcanic rocks of the Calipuy Formation and the Tantahuatay high-sulfidation epithermal Au deposit formed later in the western part of the district. The abundances of REE in igneous rocks indicate that parental magmas in the district originated from an amphibole-bearing juvenile lower crust or lithospheric mantle and evolved through amphibole fractionation over time. A similar mineralogy and lithology of other Miocene igneous rocks in the Cajamarca region suggest that they likely originated from similar sources.

Earlier magmatism in the Hualgayoc district is dioritic, with intrusions characterized by crystallization of zircon at low temperatures. Younger magmas are andesitic to rhyolitic in composition and are characterized by the crystallization of titanite with zircon. Amphibole and mineral assemblages indicate that all magmas in the district were water rich,

>3 wt %$H_2O$, and oxidized, regardless of whether or not the intrusions are altered and mineralized. Our results for the Hualgayoc district are consistent with a high-water content and high oxidation state of the causative intrusions being associated with mineralized porphyry systems, but these factors alone are not sufficient to generate porphyry and high-sulfidation ore deposits, with intrusion size and morphology, local structure and other physical factors also being critical. This likely applies to other igneous rocks in the Cajamarca region and elsewhere in the world.

## Acknowledgments

This work is part of Martin Viala's M.Sc. thesis project, supported by a Natural Science and Engineering Council of Canada Discovery Grant to Keiko Hattori. We thank Alain Mauviel for thin section preparation, Glenn Poirier for his assistance with the SEM at the University of Ottawa Micro-Analysis Laboratory, Samuel Morfin and Duane C. Petts for LA-ICP-MS assistance at the University of Ottawa, and William J. Davis and Morfin for SHRIMP analyses of zircon at the Geochronological Laboratory of the Geological Survey of Canada.

The authors acknowledge Regina Baumgartner for her support in arranging the field trips to the Hualgayoc district in July 2016 and 2017 and for obtaining the necessary permits to visit and collect samples at the Cerro Corona mine. Logistical and field support by Gold Fields La Cima S.A. at Cerro Corona mine, especially assistance by Angel Uzategui, Elber Gallardos, Paul Gomez, and Juan Sarmiento, is greatly appreciated. The authors also acknowledge Jose Trujillo from Compania de Minas Buenaventura S.A.A., as well as Kevin Heather and Stewart Redwood from Regulus Resources Inc., for their help in sampling and discussion. We thank Gold Fields La Cima S.A. for allowing us to use their intrusion map, and Regulus Resources Inc. for permitting use of their geology map for Tantahuatay. Anthony Longo and John Dilles provided thorough reviews of the manuscript, and Jeffrey Hedenquist helped to clarify the presentation.

## REFERENCES

Arribas, A.J., Jr., Hedenquist, J.W., Itaya, T., Okada, T., Concepcion, R.A., and Garcia, J.S., Jr., 1995, Contemporaneous formation of adjacent porphyry and epithermal Cu-Au deposits over 300 ka in northern Luzon, Philippines: Geology, v. 23, p. 337–340.

Bachmann, O., Dungan, M.A., and Bussy, F., 2005, Insights into shallow magmatic processes in large silicic magma bodies: the trace element record in the Fish Canyon magma body, Colorado: Contributions to Mineralogy and Petrology, v. 149, p. 338–349.

Bachmann, O., Oberli, F., Dungan, M.A., Meier, M., Mundil, R., and Fischer, H., 2007, $^{40}Ar/^{39}Ar$ and U-Pb dating of the Fish Canyon magmatic system, San Juan Volcanic field, Colorado: Evidence for an extended crystallization history: Chemical Geology, v. 236, p. 134–166.

Barckhausen, U., Ranero, C.R., Cande, S.C., Engels, M., and Weinrebe, W., 2008, Birth of an intraoceanic spreading centre: Geology, v. 36, p. 767–770. doi:10.1130/G25056A.1.

Benavides-Cáceres, V., 1956, Cretaceous system in northern Peru: Bulletin of the American Museum of Natural History, v. 108, p. 353–494.

——1999, Orogenic evolution of the Peruvian Andes: the Andean cycle: Society of Economic Geologists Special Publication 7, p. 61–107.

Black, L.P., Kamo, S.L., Allen, C.M., Aleinikoff, J.N., Davis, D.W., Korsch, R. J., and Foudoulis, C, 2003, TEMORA 1: A new zircon standard for Phanerozoic U-Pb geochronology: Chemical Geology, v. 200, p. 155–170.

Boutonnet, E., Leloup, P.H., Arnaud, N., Paquette, J.L., Davis, W.J., and Hattori, K., 2012, Synkinematic magmatism, heterogeneous deformation, and progressive strain localization in a strike-slip shear zone: The case of the right lateral Karakorum fault: Tectonics, v. 31, Tectonics vol. 31, no. 4, TC4012, https://doi.org/10.1029/2011TC003049.

Brewer, N.H., and Davis, B., 2004. Technical report, Cerro Corona project: Department of Cajamarca, Peru. (https://www.sec.gov/Archives/edgar/data/1203464/000110465904037462/a0413277_1ex99d6.htm).

Buenaventura, Tantahuatay mine 2014–2018 Au production: Buenaventura, www.buenaventura.com (accessed December 2020).

Buret, Y., Quadt, A. Von, Heinrich, C., Selby, D., Wälle, M., and Peytcheva, I., 2016, From a long-lived upper-crustal magma chamber to rapid porphyry copper emplacement: Reading the geochemistry of zircon crystals at Bajo de la Alumbrera (NW Argentina): Earth and Planetary Science Letters, v. 450, p. 120–131.

Candiotti, H., and Guerrero, T., 1997, Descubrimiento y geologia del yacimiento de oro diseminado Sipan—Cajamarca: Congreso Peruana de Geologia, 9th, Lima, Peru, August 1997, Extended Abstracts, p. 9–13.

Chelle-Michou, C., Chiaradia, M., Ovtcharova, M., Ulianov, A., and Wotzlaw, J.F., 2014, Zircon petrochronology reveals the temporal link between porphyry systems and the magmatic evolution of their hidden plutonic roots (the Eocene Coroccohuayco deposit, Peru): Lithos, v. 198–199, p. 129–140.

Chiaradia, M., Merino, D., and Spikings, R., 2009, Rapid transition to long-lived deep crustal magmatic maturation and the formation of giant porphyry-related mineralization (Yanacocha, Peru): Earth and Planetary Science Letters, v. 288, p. 505–515.

Cobbing, E.J., 1999, The Coastal batholith and other aspects of Andean magmatism in Peru: Geological Society, London, Special Publication 168, p. 111–122.

Davies, C.R., 2002, Tectono-magmatic evolution of the Cajamarca mining district, northern Peru: Ph.D. dissertation, Queensland, Australia, James Cook University, 191 p.

Davies, R.C., and Williams, P.J., 2005, The El Galeno and Michiquillay porphyry Cu-Au-Mo deposits: Geological descriptions and comparison of Miocene porphyry systems in the Cajamarca district, northern Peru: Mineralium Deposita, v. 40, p. 598–616. https://doi.org/10.1007/s00126-005-0026-6

Dunn, T., and Sen, C., 1994, Mineral/matrix partition-coefficients for ortho-pyroxene, plagioclase, and olivine in basaltic to andesitic systems—a combined analytical and experimental study: Geochimica et Cosmochimica Acta, v. 58, p. 717–733.

Eggleston, T., Reid, D, and Colquhoun, W., 2019, AntaKori Project, Cajamarca Province, Peru, NI 43-101 Technical Report https://www.regulusresources.com/site/assets/files/3992/2019_apr_15_antakori_43-101_report.pdf, accessed in May 2021.

Einaudi, M.T., Hedenquist, J.W., and Inan, E.E., 2003, Sulfidation state of fluids in active and extinct hydrothermal systems: Transitions from porphyry to epithermal environments: Society of Economic Geologists Special Publication 10, p. 285–313.

Ferry, J.M., and Watson, E.B., 2007, New thermodynamic models and revised calibrations for the Ti-in-zircon and Zr-in-rutile thermometers: Contributions to Mineralogy and Petrology, v. 154, p. 429–437.

Fu, B., Page, F.Z., Cavosie, A. J., Fournelle, J., Kita, N.T., Lackey, J.S., Wilde, S.A., and Valley, J.W., 2008, Ti-in-zircon thermometry: Applications and limitations: Contributions to Mineralogy and Petrology, v. 156, p. 197–215.

Fulignati, P., Gioncada, A., and Sbrana, A., 1999, Rare-earth element (REE) behavior in the alteration facies of the active magmatic-hydrothermal system of Vulcano (Aeolian Islands, Italy): Journal of Volcanology and Geothermal Research, v. 88, p. 325–342.

Gold Fields La Cima S.A., 2017, Cerro Corona mine, 2009–2019 Cu and Au production: https://www.goldfields.com (accessed December 2020).

Griffin L.W., 2008, GLITTER: Data reduction software for laser ablation ICP-MS: Laser Ablation ICP-MS in the Earth Sciences: Current practices and outstanding issues, p. 308–311.

Grimes, C.B., Wooden, J.L., Cheadle, M.J., and John, B.E., 2015, "Fingerprinting" tectono-magmatic provenance using trace elements in igneous zircon: Contributions to Mineralogy and Petrology, v. 170, p. 1–26.

Gustafson, L.B., Vidal, C.E., Pinto, R., and Noble, D.C., 2004, Poryhyry-epithermal transition, Cajamarca region, northern Peru: Society of Economic Geologists Special Publication 11, p. 279–300.

Harvey, B., Myers, S., and Klein, T., 1999, Yanacocha gold district, northern Peru: PacRim '99 Congress, Bali, Indonesia, October 10–13, Australasian Institute of Mining and Metallurgy, Proceedings, p. 445–459.

Hattori, K., 2018, Porphyry copper potential in Japan based on magmatic oxidation state: Resource Geology, v. 68, p. 126–137.

Hawthorne, F.C., Oberti, R., Harlow, G.E., Maresch, W.V., Martin, R.F., Schumacher, J.C., and Welch, M.D., 2012, Nomenclature of the amphibole supergroup: American Mineralogist, v. 97, p. 2031–2048.

Hedenquist, J.W., Arribas, A., and Reynolds, T. J., 1998, Evolution of an intrusion-centered hydrothermal system: Far Southeast-Lepanto porphyry and epithermal Cu-Au deposits, Philippines: Economic Geology, v. 93, p. 373–404.

Hoffman, J.F., and Long, J.V.P., 1984, Unusual sector zoning in Lewisian zircons: Mineralogical Magazine, v. 48, p. 513–517.

Ishihara, S., 1977, The magnetite-series and ilmenite-series granitic rocks: Mining Geology, v. 27, p. 293–305.

James, J., 1998, Geology, alteration and mineralization of the Cerro Corona Porphyry copper-gold deposit, Cajamarca province, Peru: Ph.D. dissertation, British Columbia, Canada, University of British Columbia, 249 p.

Jochum, K.P., Weis, U., Stoll, B., Kuzmin, D., Yang, Q., Raczek, I., Jacob, D.E., Stracke, A., Birbaum, K., Frick, D.A., Günther, D., and Enzweiler, J., 2011, Determination of reference values for NIST SRM 610–617 glasses following ISO guidelines: Geostandards and Geoanalytical Research, v. 35, p. 397–429.

Kobylinski, C., Hattori, K., Smith, S., and Plouffe, A., 2020, Protracted magmatism and mineralized hydrothermal ectivity at the Gibraltar porphyry copper-molybdenum deposit, British Columbia: Economic Geology, v. 115, p. 1119–1136.

Kohn, M.J., 2017, Titanite petrochronology: Reviews in Mineralogy and Geochemistry, v. 83, p. 419–441.

Laughlin, A.W., Damon, P.E., and Watson, B.N., 1968, Potassium-argon data from Toquepala and Michiquillay, Peru: Economic Geology, v. 63, p. 166–168.

Llosa, F., Lescuyer, J.L., and Milesi, J.P., 1996, Minas Congas: descubrimiento, exploracion y marco geologico de los porfidos Au-Cu en la region de Cajamarca: Segundo Simposio Internacional del Oro, Comite Aurifero, Sociedad Nacional de Mineria y Petroleo, Lima, p. 275–283.

Llosa, F.T., Veliz, J.M., and Georgel, J.M.P., 1999, Los Porfidos Au-Cu Minas Congas: Historia del descubrimiento y exploracion entre 1992–1998: Primer Volumen de Monografías de Yacimientos Minerales Peruanos, Volumen Luis Hochschild Plaut, ProExplo '99, Instituto de Ingenieros de Minas del Perú, p. 177–195.

Loader, M.A., Wilkinson, J.J., and Armstrong, R.N., 2017, The effect of titanite crystallisation on Eu and Ce anomalies in zircon and its implications for the assessment of porphyry Cu deposit fertility: Earth and Planetary Science Letters, v. 472, p. 107–119.

Longo, A.A., 2005, Evolution of volcanism and hydrothermal activity in the Yanacocha mining district, northern Perú: Ph.D. dissertation, Corvallis, Oregon State University, 469 p.

Longo, A.A., Dilles, J.H., Grunder, A.L., and Duncan, R., 2010, Evolution of calc-alkaline volcanism and associated hydrothermal gold deposits at Yanacocha, Peru: Economic Geology, v. 105, p. 1191–1241.

Longridge, J., 2016, Evolution of hydrothermal alteration facies at the Cerro Corona Cu-Au porphyry deposit, northern Peru: Ph.D. dissertation, London, Imperial College London, 300 p.

Loucks, R.R., Fiorentini, M.L., and Henríquez, G. J., 2020, New magmatic oxybarometer using trace elements in zircon: Journal of Petrology, v. 61, p. 1–30.

Ludwig, K.R., 2003, Isoplot 3.00: A geochronological toolkit for Microsoft Excel: Berkeley Geochronology Center Special Publication, v. 4, p. 70.

Macfarlane, A.W., 1989, Lead, sulfur and strontium isotopes in the Hualgayoc area, Peru, and lead isotope provinces of the central Andes: Ph.D. dissertation, Cambridge, Harvard University, 374 p.

Macfarlane, A.W., and Petersen, U., 1990, Pb isotopes of the Hualgayoc area, northern Peru: Implications for metal provenance and genesis of a Cordilleran polymetallic mining district: Economic Geology, v. 85, p. 1303–1327.

Macfarlane, A.W., Prol-Ledesma, R.M., and Conrad, M.E., 1994, Isotope and fluid inclusion studies of geological and hydrothermal processes, northern Peru: International Geology Review, v. 36, p. 645–677.

McDonough, W.F., and Sun, S.S., 1995, The composition of the Earth: Chemical Geology, v. 120, p. 223–253.

Mégard, F., 1984, The Andean orogenic period and its major structures in central and northern Peru: Journal of the Geological Society, v. 141, p. 893–900.

Mišković, A., Spikings, R.A., Chew, D.M., Košler, J., Ulianov, A., and Schaltegger, U., 2009, Tectonomagmatic evolution of Western Amazonia: Geochemical characterization and zircon U-Pb geochronologic constraints from the Peruvian Eastern Cordilleran granitoids: Bulletin of the Geological Society of America, v. 121, p. 1298–1324.

Moore, G., Vennemann, T., and Carmichael, I.S.E., 1995, Solubility of water in magmas to 2 kbar: Geology, v. 23, p. 1099–1102.

Mukasa, S.B., and Tilton, G.R., 1984, Phanerozoic plutonism in the Peruvian Andes, *in* Harmon R.S., and Barreiro B.A., ed., Andean magmatism: Boston, MA, Birkhäuser Basel, p. 180–189.

Naney, M.T., 1983, Phase equilibria of rock-forming ferromagnesian silicates in granitic systems: American Journal of Science, v. 283, p. 993–1033.

Noble, D.C., and McKee, E.H., 1997, The Miocene metallogenic belt of central and northern Peru: Congreso Peruano de Geología, IX, Resúmenes Extendidos, Sociedad Geológica del Perú, Lima, Perú, v. 1, p. 115–119.

——1999, The Miocene metallogenic belt of central and northern Peru: Society of Econornic Geologists Special Publication 7, p. 155–194.

Noble, D.C., McKee, E.H., Mourier, T., and Megard, F., 1990, Cenozoic stratigraphy, magmatic activity, compressive deformation, and uplift in northern Peru: Geological Society of America Bulletin, v. 102, p. 1105–1113.

Noble, D.C., Vidal, C.E., Perelló, J., and Rodríguez, O.P., 2004, Space-time relationships of some porphyry Cu-Au, epithermal Au, and other magmatic-related mineral deposits in northern Perú: Society of Economic Geology Special Publication 11, p. 313–318.

Pardo-Casas, F., and Molnar, P., 1987, Relative motion of the Nazca (Farallon) and South American plates since Late Cretaceous time: Tectonics, v. 6, p. 233–248.

Prihar, D., 1998, Geology map of the Hualgayoc district, Tantahuatay project: Unpublished report, Cia. Minera Coimolache, S.A., scale 1:2,500.

Prowatke, S., and Klemme, S., 2006, Trace element partitioning between apatite and silicate melts: Geochimica et Cosmochimica Acta, v. 70, p. 4513–4527.

Redwood, S.D., Heather, K.B., Gamarra,m H., and Mamani, C., 2017, The AntaKori Cu-Au-Ag skarn project, Cajamarca, northern Peru [ext. abs.]: ProExplo 2017, Lima, Peru, Extended Abstract.

Regulus Resources, Inc., 2021, AntaKori project, 2019 Cu and Au resources: https://regulusresources.com/projects/resource/ (accessed December 2020)

Richards, J.P., 2014, The oxidation state, and sulfur and Cu contents of arc magmas: Implications for metallogeny: Lithos, v. 233, p. 27–45.

Richards, J.P., and Kerrich, R., 2007, Adakite-like rocks: Their diverse origins and questionable role in metallogenesis: Economic Geology, v. 102, p. 537–576.

Ridolfi, F., Renzulli, A., and Puerini, M., 2010, Stability and chemical equilibrium of amphibole in calc-alkaline magmas: An overview, new thermobarometric formulations and application to subduction-related volcanoes: Contributions to Mineralogy and Petrology, v. 160, p. 45–66.

Scherrenberg, A.F., Jacay, J., Holcombe, R.J., and Rosenbaum, G., 2012, Stratigraphic variations across the Marañón fold-thrust belt, Peru: Implications for the basin architecture of the West Peruvian trough: Journal of South American Earth Sciences, v. 38, p. 147–158.

Sillitoe, R.H., 2010, Porphyry copper systems: Economic Geology, v. 105, p. 3–41.

Sillitoe, R.H., and Hedenquist, J.W., 2003, Linkages between volcanotectonic settings, ore-fluid compositions, and epithermal precious metal deposits: Society of Economic Geologists Special Publication 10, p. 315–343.

Sisson, T.W., 1994, Hornblende-melt trace-element partitioning measured by ion microprobe: Chemical Geology, v. 117, p. 331–344.

Sláma, J., Košler, J., Condon, D.J., Crowley, J.L., Gerdes, A., Hanchar, J.M., Horstwood, M.S.A., Morris, G.A., Nasdala, L., Norberg, N., Schaltegger, U., Schoene, B., Tubrett, M.N., and Whitehouse, M.J., 2008, Plešovice zircon—a new natural reference material for U-Pb and Hf isotopic microanalysis: Chemical Geology, v. 249, p. 1–35. https://doi.org/10.1016/j.chemgeo.2007.11.005

Smythe, D.J., and Brenan, J.M., 2016, Magmatic oxygen fugacity estimated using zircon-melt partitioning of cerium: Earth and Planetary Science Letters, v. 453, p. 260–266.

Spencer, C.J., Kirkland, C.L., and Taylor, R.J., 2016, Strategies towards statistically robust interpretations of in situ U-Pb zircon geochronology: Geoscience Frontiers, v. 7, p. 581–589.

Terakado, Y., and Fujitani, T., 1998, Behavior of the rare earth elements and other trace elements during interactions between acidic hydrothermal solutions and silicic volcanic rocks, southwestern Japan: Geochimica et Cosmochimica Acta, v. 62, p. 1903–1917.

Tiepolo, M., Oberti, R., Zanetti, A., and Foley, S. F., 2007, Trace-element partitioning between amphibole and silicate melt: Reviews in Mineralogy and Geochemistry, v. 67, p. 417–451.

Trail, D., Bruce Watson, E., and Tailby, N.D., 2012, Ce and Eu anomalies in zircon as proxies for the oxidation state of magmas: Geochimica et Cosmochimica Acta, v. 97, p. 70–87.
Uzategui-Obando, A., 2016, Mineralizacion y fases intrusivas en el porfido de cobre-oro (molibdeno) de Cerro Corona: Congreso Peruano de Geologia, 18th, https://www.sgp.org.pe/congreso2016/inicio/
Van Dongen, M., Weinberg, R.F., and Tomkins, A. G., 2010, REE-Y, Ti, and P remobilization in magmatic rocks by hydrothermal alteration during Cu-Au deposit formation: Economic Geology, v. 105, p. 763–776.
Vermeesch, P., 2018, IsoplotR: A free and open toolbox for geochronology: Geoscience Frontiers, v. 9, p. 1479–1493.
Viala, M., and Hattori, K., 2021, Hualgayoc mining district, northern Peru: Testing the use of zircon composition in exploration for porphyry-type deposits: Journal of Geochemical Exploration, v. 223, p. 106725, doi: https://doi.org/10.1016/j.gexplo.2021.106725
Wang, R., Richards, J.P., Hou, Z., Yang, Z., Gou, Z., and Dufrane, S.A., 2014, Increasing magmatic oxidation state from Paleocene to Miocene in the eastern Gangdese belt, Tibet: Implication for collision-related porphyry Cu-Mo ± Au mineralization: Economic Geology, v. 109, p. 1943–1965.
Watson, E.B., and Harrison, T.M., 1983, Zircon saturation revisited: Temperature and composition effects in a variety of crustal magma types: Earth and Planetary Science Letters, v. 64, p. 295–304.
Watson, E.B., Wark, D.A., and Thomas, J.B., 2006, Crystallization thermometers for zircon and rutile: Contributions to Mineralogy and Petrology, v. 151, p. 413–433.
Whalen, J.B., Davis, W.J., and Anderson, R.A., 2017, Temporal and geochemical evolution of the Guichon Creek batholith and Highland Valley porphyry copper district, British Columbia: Implications for generation and tectonic setting of porphyry systems: Geological Survey of Canada Open File 8334 , 45 p., doi: 10.4095/306147
Wiedenbeck M., Allé P., Corfu F., Griffin W. L, Meier M., Oberli F., von Quadt A., Roddick J.C., and Spiegel W., 1995, Three natural zircon standards for U-Th-Pb, Lu-Hf, trace element and REE analyses: Geostandards Newsletter, v. 19, p. 1–23.
Wilson, J.J., 1963, Cretaceous stratigraphy of Central Andes of Peru: American Association of Petroleum Geologists Bulletin, v. 47, p. 1–34.
——1984, Geología de los cuadrángulos de Jayanca, Incahuasi, Cutervo, Chiclayo, Chongoyape, Chota, Celendín, Pacasmayo y Chepén: Instituto Geológico Minero y Metalúrgico, Lima, Boletín 38 serie A, 104 p.
Wones, D.R., 1989, Significance of the assemblage titanite + magnetite + quartz in granitic rocks: American Mineralogist, v. 74, p. 744–749.
Yanacocha district, Au and Cu reserves: Mining Data Solutions, www.miningdataonline.com (accessed December 2020).

**Martin Viala** obtained a B.Sc. degree at the Université du Québec à Montréal in 2016 and an M.Sc. degree from the University of Ottawa in 2020. He moved from France to Madagascar while a youngster, where he developed a keen interest in minerals and gems; this eventually led to his attaining a gemology diploma from the Gemmological Association of Great Britain. After working as an exploration geologist with Walbridge Mining Company in northern Quebec, Martin relocated to Thailand to work with Greenland Ruby to follow his interest in gem minerals.

**Keiko Hattori** is professor at the University of Ottawa, Canada, where she has taught geochemistry and mineral deposits since 1983, following a Ph.D. degree at the University of Tokyo. Keiko examines element transfer in subduction zones and mineralized hydrothermal systems. She and her students have studied a variety of mineral deposits and their exploration methods, including epithermal and orogenic gold, porphyry copper, unconformity-type U, and kimberlites. Keiko is an elected Fellow of the Mineralogical Society of America and Fellow of the Royal Society of Canada and is currently associate editor of *Nature Scientific Reports* and *Economic Geology*.

# APPENDIX 1

## Analytical Methods

### *A1.1 Bulk-rock analyses*

Loss on ignition (LOI) was measured at the University of Ottawa, using 1 to 5 g of pulverized samples after heating samples at 1,050°C for 2 h. The abundance of major elements, Sr and Zr, were measured using a Rigaku Supermini 200 wavelength dispersive X-ray fluorescence spectrometer (XRF) on fused glass of pulverized samples mixed with lithium metaborate and lithium tetraborate at the University of Ottawa. Accuracy obtained from measured values of certified reference GSP-2 is better than 99% for major elements and 95% for minor elements.

The abundances of trace elements, including REE, were determined by Actlabs (analytical code 4LITHOS) in Ancaster, Ontario, Canada. Fused samples with sodium peroxide were dissolved in nitric and hydrochloric acids. The resulting solutions were diluted and analyzed using an Agilent 7900 inductively coupled plasma-mass spectrometer (ICP-MS) and a Varian 735ES inductively coupled plasma-optical emission spectrometer (ICP-OES). Precision of the analysis was determined by comparing duplicate samples. Accuracy was calculated by comparing measured values to certified values NIST 696, NCS DC86303, NCS DC86314, OREAS 101a, OREAS 13b, OREAS 131a, GXR-1, GBW 07239, MP-1b, and CCU-1e. Most elements show an accuracy better than 90%. Bulk-rock compositional data are listed in Appendix 2, Table A2-2.

### *A1.2 Zircon analyses for compositions and U-Pb ages*

Samples were crushed and separated into several size fractions using sieves of 500-, 210-, 125-, and 53-µm mesh size. Zircon grains were concentrated from the 210- to 125 and 125- to 53-µm fractions, using conventional magnetic and density techniques. Clear pink grains were handpicked under a binocular microscope and mounted into an epoxy resin. Grains were examined under transmitted light microscope to check the presence of fractures and minerals inclusions such as apatite and plagioclase, which are common in most of our grains. Inclusion-free grains were examined with a cathodoluminescence detector attached to a scanning electron microscope (SEM-CL) at the University of Ottawa MicroAnalysis Laboratory. Transparent zircon grains without alteration, in-

clusions, and fractures were selected for the analysis. Zircon grains showing sector zoning were not selected for trace element analysis as they have highly heterogeneous compositions (Hoffman and Long, 1984). SEM-CL images of analyzed zircon grains are shown in Appendix 2, Figure A2-3. Optical properties and textures of analyzed zircon are described in Viala and Hattori (2021).

Trace element abundances were determined at the University of Ottawa, using an Agilent 7700x ICP-MS coupled with a Photon Machines Analyte Excite 193-nm excimer laser. For each grain, the analysis area was located as close as possible to the rim in order to avoid the inclusion-rich center of the grains as well as potential inherited cores. Inherited cores are rare but easily identified due to corroded outline of the cores. Reference materials NIST 612, BCR, GSEG1, BCR2G, and GSD1G (Jochum et al., 2011), and 91500 zircon (Wiedenbeck et al., 1995) were analyzed for every seven unknown zircon samples. Contamination by minute mineral inclusions was monitored using $^{42}$Ca, $^{54}$Fe, $^{31}$P, $^{88}$Sr, and $^{139}$La. Analyses with a sharp increase in Ca, Fe, P, Sr, and La were discarded. Raw data were reduced using the GLITTER software (Griffin, 2008) with NIST612 reference material as the primary standard. Trace element concentrations were obtained based on the count ratios of the element to $^{29}$Si and the composition of NIST612 (72.1 wt % $SiO_2$; Jochum et al., 2011) and the stoichiometric zircon $SiO_2$ content (31.57 wt %). Reference materials BCR-G and GSEG were used as secondary standards, and 91500 and Plešovice zircon were used to validate the analytical data. The instrument set-up and analytical method are essentially identical to those described in detail by Kobylinski et al. (2020). A summary of LA-ICP-MS trace elements in zircon is listed in Appendix 2, Table A2-3. Detailed metadata for LA-ICPMS trace element analysis sessions are described in Appendix 2, Table A2-4.

U-Pb ages of zircon from all samples except those from the Cerro Corona Intrusive Complex were obtained on separate runs using the same Agilent 7700x ICP-MS coupled with a Photon Machines Analyte Excite 193-nm excimer laser. For each grain, the analysis area was located as close as possible to the rim in order to avoid the inclusion-rich center of the grains as well as potential older inherited cores. Contamination by minute mineral inclusions was monitored using $^{140}$Ce. Analyses with a sharp increase in the counts of Ce were discarded. Data reduction and correction for instrument drift were processed using the GLITTER software, with 91500 zircon (1065 ± 0.3 Ma; Wiedenbeck et al., 1995) used as internal standard. Individual zircon ages were calculated from $^{206}$Pb/$^{238}$U ratio using the IsoplotR software (Vermeesch, 2018), a modified program of the original *Isoplot* program by Ludwig (2003). Standard zircon 91500 and Plešovice zircon (337.13 ± 0.37 Ma; Sláma et al., 2008) were used as external standards for validation of calculated ages. LA-ICP-MS zircon U/Pb data are listed in Appendix 2, Table A2-5. Detailed metadata for LA-ICP-MS U-Pb analysis sessions are described in Appendix 2, Table A2-4.

U-Pb ages of zircon from intrusive phases 1, 4, 5, and 6 of the Cerro Corona Intrusive Complex were determined with the SHRIMPII at the Geochronological Laboratory of the Geological Survey of Canada. Selected zircons were mounted with standards FCT (Bachmann et al., 2007), Temora (Black et al., 2003), and GCS 6266 zircon (Whalen et al., 2017), with respective ages of 28.402 ± 0.023, 416.5 ± 0.22 and 559 Ma. Epoxy mount was polished and coated with gold. Individual zircon ages were calculated from $^{207}$Pb-corrected $^{206}$Pb/$^{238}$U ratio using the IsoplotR software (Vermeesch, 2018). The instrumental and analytical methods are described in Boutonnet et al. (2012) and Whalen et al. (2017). SHRIMP zircon U/Pb data summary is given in Appendix 2, Table A2-6.

Ages of samples were calculated from the weighted mean of zircon $^{206}$Pb/$^{238}$U ages, using the IsoplotR software. The software automatically removed outlier zircon during the calculation. The Concordia age of samples was also plotted to identify discordant spots. The weighted mean plots, Concordia plots, and number of spots used for the age calculation are shown in Appendix 2, Figure A2-4. Due to the very low abundance of $^{235}$U in our zircon, the analytical uncertainties of the $^{207}$Pb/$^{235}$U ratios are very large. Therefore, we did not use the Concordia ages in our study. Seven weighted mean ages (sample Tanta-357, Tanta-358, CNG-1, CJ, LG, Anta-8, and 25-6) out of 25 have high MSWD, between 2.65 to 17.7 (Fig. A2-4, App. 2), due to the large spread of zircon $^{206}$Pb/$^{238}$U ages around the mean for these samples. As we do not have any evidence that any of these analyses are of zircon ante- or xenocrysts, we did not manually cull data to achieve an acceptable MSWD for these seven samples, as recommended by Spencer et al. (2016).

### *A1.3 Amphibole composition*

Igneous amphibole grains from the San Nicolas intrusion and the Coymolache sill were examined, using backscatter SEM to select three grains from the former and four from the latter. For each grain we selected areas for analysis that have the same shade of gray in backscatter images that seemed representative of the igneous composition of the grains. We avoided areas that showed a sign of alteration and irregular to patchy zoning. The compositions of each grain were quantitatively determined with a JEOL 8230 electron probe microanalyzer at the University of Ottawa. Analytical conditions included accelerating voltage of 15 kV, beam current of 20 nA, and a focused beam size of 5 µm. Element abundances were acquired using analyzing crystals LIF for Fe $k_\alpha$, Mn $k_\alpha$, PETJ for K $k_\alpha$, Ca $k_\alpha$, PETL for Ti $k_\alpha$, Cr $k_\alpha$, Cl $k_\alpha$, and TAP for Si $k_\alpha$, Mg $k_\alpha$, Al $k_\alpha$, F $k_\alpha$, Na $k_\alpha$. The standards were albite for Na $k_\alpha$ diopside #1 for Ca $k_\alpha$, Mg $k_\alpha$, sanidine for Al $k_\alpha$, Si $k_\alpha$, K $k_\alpha$, hematite for Fe $k_\alpha$, rutile for Ti $k_\alpha$, tephroite for Mn $k_\alpha$, fluorite for F $k_\alpha$, tugtupite for Cl $k_\alpha$, and chromite for Cr $k_\alpha$. The analytical procedure is essentially identical to that described in detail by Kobylinski et al. (2020). Amphibole compositional data and detailed metadata for analyses are given in Appendix 2, Table A2-7.